Ab initio analysis of the tight-binding parameters and magnetic interactions in Na_2IrO_3

Kateryna Foyevtsova,[1] Harald O. Jeschke,[1] I. I. Mazin,[2] D. I. Khomskii,[3] and Roser Valentí[1]
[1]*Institut für Theoretische Physik, Goethe-Universität Frankfurt, 60438 Frankfurt am Main, Germany*
[2]*Code 6393, Naval Research Laboratory, Washington, DC 20375, USA*
[3]*II. Physikalisches Institut, Universität zu Köln, Zülpicher Strasse 77, 50937 Köln, Germany*
(Received 25 March 2013; revised manuscript received 31 May 2013; published 8 July 2013)

By means of density functional theory (DFT) calculations [with and without inclusion of spin-orbit (SO) coupling] we present a detailed study of the electronic structure and corresponding microscopic Hamiltonian parameters of Na_2IrO_3. In particular, we address the following aspects: (i) We investigate the role of the various structural distortions and show that the electronic structure of Na_2IrO_3 is exceptionally sensitive to structural details. (ii) We discuss both limiting descriptions for Na_2IrO_3—quasimolecular orbitals (small SO limit, itinerant) versus relativistic orbitals (large SO limit, localized)—and show that the description of Na_2IrO_3 lies in an intermediate regime. (iii) We investigate whether the nearest neighbor Kitaev-Heisenberg model is sufficient to describe the electronic structure and magnetism in Na_2IrO_3. In particular, we verify the recent suggestion of an antiferromagnetic Kitaev interaction and show that it is not consistent with actual or even plausible electronic parameters. Finally, (iv) we discuss correlation effects in Na_2IrO_3. We conclude that while the Kitaev-Heisenberg Hamiltonian is the most general expression of the quadratic spin-spin interaction in the presence of spin-orbit coupling (neglecting single-site anisotropy), the itinerant character of the electrons in Na_2IrO_3 makes other terms beyond this model (including, but not limited to, 2nd and 3rd neighbor interactions) essential.

DOI: 10.1103/PhysRevB.88.035107 PACS number(s): 75.10.Jm, 71.70.Ej, 71.15.Mb

I. INTRODUCTION

The electronic and magnetic behavior of layered $5d$ transition metal oxides[1] has been a subject of intensive discussion in the last years. Particularly exciting has been the suggestion by the authors of Ref. 2 that hexagonal iridates such as Na_2IrO_3 are a realization of the nearest neighbor Kitaev-Heisenberg (nnKH) model:

$$H_{ij}^{(\gamma)} = 2K S_i^{\gamma} S_j^{\gamma} + J\mathbf{S}_i \cdot \mathbf{S}_j. \quad (1)$$

This proposal is based on the premise that spin-orbit (SO) coupling is the most important energy scale for the description of these systems so that Ir $5d$ t_{2g} orbitals are written in terms of $j_{\text{eff}} = 1/2$ and $j_{\text{eff}} = 3/2$ relativistic orbitals, with the Kramers doublet $j_{\text{eff}} = 1/2$ represented by the operator $S = 1/2$. The combination of Kitaev and Heisenberg terms leads to a complex phase diagram with various magnetic and spin-liquid phases.[2–4] Obviously, some of these properties can only manifest themselves when the Kitaev term dominates or is at least comparable to the Heisenberg term. Also, other possible contributions, such as magnetic anisotropy, ring exchange, or biquadratic exchange, to mention a few, may alter the phase diagram and the properties of the model considerably. Most importantly, while the Kitaev-Heisenberg expression is the most general fully symmetric expression for anisotropic pairwise magnetic interactions in the second order in spin in the presence of SO coupling (just as the Heisenberg exchange represents the same in the isotropic nonrelativistic case), it is not necessarily short ranged in the presence of considerable itinerancy.

So far, essentially all analyses of the nnKH model for Na_2IrO_3 have been performed in the localized limit, where an assembly of weakly interacting relativistic atomic orbitals is assumed to be a good starting approximation. On the other hand, first-principles calculations suggest considerable delocalization of electrons over individual Ir hexagons building quasimolecular orbitals (QMOs).[5] The associated "itinerant" energy scale (the bandwidth) is ≈1.5 eV, to be compared to the single-site spin-orbit splitting scale[6] $(3/2)\lambda \approx 0.7$ eV and the Hubbard and Hund's rule correlation energy scale of $U - J_{\text{H}} \approx 0.5$–1 eV. This makes the entire premise of the nnKH model questionable. At the same time, it has also been pointed out[7,8] that the nnKH model with the addition of the 2nd and 3rd neighbors Heisenberg interaction is easier to reconcile with the experimental data. Such relatively long-range exchange interaction is another hallmark of considerable itinerancy (here and below, when we speak of itinerancy, we imply mostly delocalization over Ir_6 rings, but not necessarily over the entire crystal).

In the present work we revisit and discuss the validity of both limiting descriptions for Na_2IrO_3: itinerant (QMO picture) versus localized ($j_{\text{eff}} = 1/2$ Kramers doublet). To this end, we perform a thorough analysis of the electronic properties of Na_2IrO_3 within *nonrelativistic* and *relativistic* density functional theory (DFT) and derive, using projection on Wannier functions, the relevant hopping parameters and show that QMOs are naturally obtained as linear combinations of Ir t_{2g} Wannier functions. We discuss the relation between the quasimolecular orbital and the relativistic orbital, j_{eff}, representations and show that the behavior of Na_2IrO_3 lies in between a fully localized and fully itinerant description. Finally, the parametrization of the electronic band structure allows us to provide realistic estimates for the model parameters in the localized nnKH model. We thus investigate whether we are close to a regime where the Kitaev interaction plays a decisive role or not.

Quite unexpectedly, we find that Na_2IrO_3 is an example of a material where minor details of the crystal structure can dramatically affect the electronic structure, and simple guessing of the band structure parameters, or estimating them from simplified crystallographic models (so far all model calculations for this compound were utilizing one or the other

approach), can be exceptionally misleading. In fact some of the models energetically discussed in the community, while of undeniable theoretical appeal, are not even qualitatively close to the actual parameter range in Na_2IrO_3.

While this particular compound is very intriguing and has been enjoying extraordinary popularity lately, we want to emphasize that this strong dependence of the electronic properties on details of the crystal structure is an important result, whose relevance goes beyond specifically Na_2IrO_3 and is likely true for many other materials based on honeycomb transition-metal layers.

The paper is organized as follows. In Sec. II we review the crystal structure and magnetic properties of Na_2IrO_3. In Sec. III we provide details of the DFT calculations and the projector method. In Sec. IV we present the results of the electronic structure analysis without inclusion of spin-orbit coupling and analyze the role of the structural distortions in Na_2IrO_3. In Sec. V we investigate the role of spin-orbit coupling and discuss the relation between the QMOs and the relativistic orbitals (j_{eff}). In this context, we discuss whether the existing experimental situation can distinguish between the DFT description (with the resulting itinerancy) and localized ($j_{\text{eff}} = 1/2$) models. We proceed with an analysis of the single-site magnetic anisotropy in Na_2IrO_3 and find it to be relevant (pure $j_{\text{eff}} = 1/2$ states do not have any single-site anisotropy). In Sec. VI we provide *ab initio*–derived estimates for the parameters appearing in the Kitaev and Heisenberg terms in Na_2IrO_3 and discuss the validity of the nnKH model by considering the experimentally observed magnetic order and attempts to explain it from a local point of view. Finally in Sec. VII we present our conclusions.

II. CRYSTAL STRUCTURE AND MAGNETIC PROPERTIES OF Na_2IrO_3

Na_2IrO_3 crystallizes in the monoclinic space group $C\,2/m$ (No. 12)[8] (see Fig. 1) and consists of Ir honeycomb layers [Fig. 1(b)] stacked along the monoclinic **c** axis [Fig. 1(a)] with an in-plane offset along **a**. Na ions occupy both the interlayer positions and 1/3 of the in-plane positions at the centers of Ir hexagons. This structure can be visualized as proceeding from $NaIrO_2$ with a CdI_2 structure with triangular IrO_2 layers. In these layers 1/3 of the in-plane iridium atoms are substituted by extra Na, i.e., its formula can be written as $Na(Na_{1/3}Ir_{2/3})O_2$, which, multiplied by 3/2, gives the usual formula of Na_2IrO_3.[9]

An idealized crystal structure of this kind corresponds to having all nearest neighbor (NN) Ir-Ir and NN Ir-O distances equal and Ir-O-Ir angles of 90 degrees. The experimental structure of Na_2IrO_3 departs from the idealized case and shows a few distortions: (i) orthorhombic distortion that introduces inequality among NN Ir-Ir distances and among NN Ir-O distances, (ii) IrO_6 octahedra rotations that place O atoms on the faces of a cube containing an Ir hexagon (see Fig. 2 of Ref. 5), and (iii) trigonal distortion which is a compression of the IrO_6 octahedra in the **c** direction that induces a departure from 90 degrees of the Ir-O-Ir angles. In Sec. IV we will discuss the effect of these distortions on the electronic structure of Na_2IrO_3.

As shown by transport, optical, and high-energy spectroscopy studies,[10,11] Na_2IrO_3 is an insulator with an energy gap E_g of 340 meV. Magnetic susceptibility measurements indicate a Curie-Weiss behavior at high temperatures with a Curie-Weiss temperature $\Theta_{CW} = -116$ K and an effective Ir moment $\mu_{\text{eff}} = 1.82\mu_B$. Na_2IrO_3 orders antiferromagnetically below $T_N = 15$ K with an ordered magnetic moment $\mu_{ord} \sim 0.2\mu_B$. The fact that T_N is much smaller than Θ_{CW} may be a signature of frustration, but it may be also caused by the itinerancy of Ir $5d$ electrons[5] as will be discussed in Sec. VI.

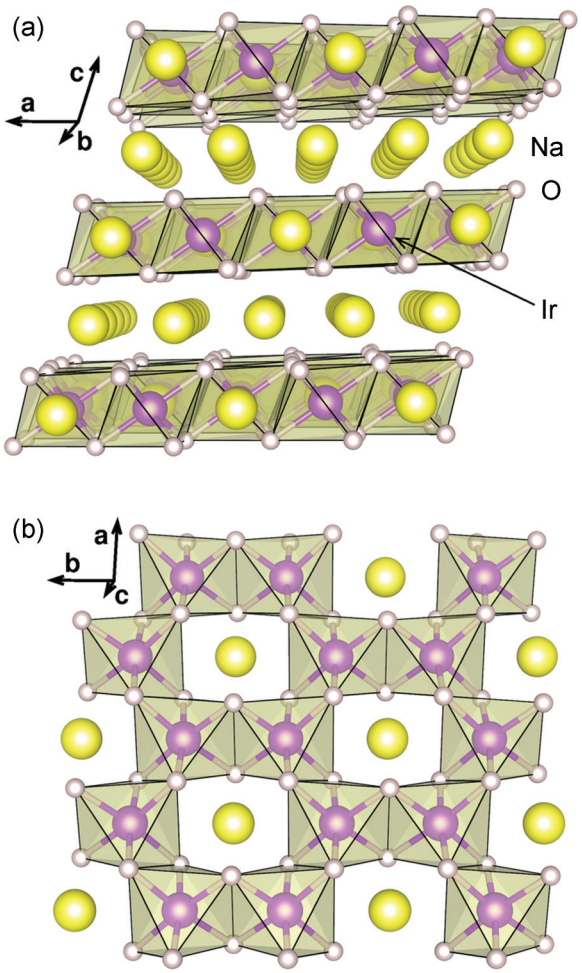

FIG. 1. (Color online) Crystal structure of Na_2IrO_3. (a) Projection on the ac plane and (b) projection on the ab plane.

The magnetic pattern observed experimentally[8] corresponds to a zigzag ordering, in contrast to the prediction of

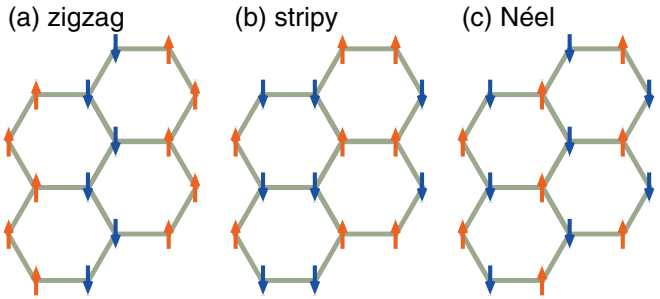

FIG. 2. (Color online) Possible antiferromagnetic patterns in a honeycomb lattice.

a stripe order by the nnKH model[2] (see Fig. 2). Recently, Chaloupka *et al.*[4] argued that such a zigzag ordering can be also obtained by the nnKH model, when one correctly includes all the terms contributing to NN Ir-Ir exchange. In Sec. V, we will discuss this proposition in more detail.

III. METHOD

In this work we perform DFT calculations using the linearized augmented plane wave (LAPW) method as implemented in the full-potential code WIEN2k.[12] We employ the Perdew-Burke-Ernzerhof generalized gradient approximation[13] to the DFT exchange-correlation functional and set the basis-size controlling parameter $RK_{\max}$[14] to 7. We consider a mesh of 500 $\mathbf{k}$ points in the first Brillouin zone. Relativistic effects are treated within the second variational approach. Convergence with respect to relevant parameters (the $\mathbf{k}$-point mesh, the $RK_{\max}$ and the second variational energy cutoff, etc.) has been carefully checked.

A. Calculation of hopping integrals

In order to be able to discuss various Ir-Ir 5*d* processes, we parametrize our nonrelativistic DFT results in terms of a tight-binding (TB) model where the TB Ir 5*d* hopping parameters are obtained through the Wannier function projection formalism proposed in Ref. 15 and generalized to molecular Wannier functions in Ref. 16. We first construct Wannier function projectors $P^{\alpha}_{m\nu}(\mathbf{k})$ for the three t_{2g} Ir 5*d* orbitals and calculate the TB Hamiltonian $H^{\mathrm{TB}}(\mathbf{k})$ (in matrix form) via

$$H^{\mathrm{TB}}(\mathbf{k}) = P(\mathbf{k})D(\mathbf{k})P^{\dagger}(\mathbf{k}), \tag{2}$$

where $D(\mathbf{k})$ is a diagonal matrix of Ir 5*d* t_{2g} Bloch eigenvalues and the matrix $P(\mathbf{k})$ is formed by the projectors $P^{\alpha}_{m\nu}(\mathbf{k})$. Here, indices α, m, and ν run over equivalent Ir atoms in the unit cell, Ir t_{2g} orbitals, and Bloch bands, respectively. Na_2IrO_3 has two Ir per unit cell and only the six Ir t_{2g} bands near the Fermi level E_{F} are considered in the construction of projectors.

We calculate the hopping integral $t^{mm'}_{\alpha-\mathbf{R},\alpha'-\mathbf{R}'}$ between orbital m on Ir atom α in the unit cell at a distance $\mathbf{R}$ from a reference unit cell and orbital m' on Ir atom α' in the unit cell at a distance $\mathbf{R}'$ from a reference unit cell by integrating $H^{\mathrm{TB}}(\mathbf{k})$ over $N_{\mathbf{k}}$ $\mathbf{k}$ vectors in the first Brillouin zone:

$$t^{mm'}_{\alpha-\mathbf{R},\alpha'-\mathbf{R}'} = \frac{1}{N_{\mathbf{k}}}\sum_{\mathbf{k}} H^{\mathrm{TB}}_{\alpha m,\alpha' m'}(\mathbf{k})e^{-i\mathbf{k}(\mathbf{R}-\mathbf{R}')}, \tag{3}$$

where $H^{\mathrm{TB}}_{\alpha m,\alpha' m'}(\mathbf{k})$ are the matrix elements of $H^{\mathrm{TB}}(\mathbf{k})$. Correspondingly, the diagonal matrix elements $t^{mm}_{\alpha\alpha}$ give the on-site energies.

B. Construction of quasimolecular projectors

As was argued in Ref. 5, the most natural description of the electronic structure of Na_2IrO_3 is in terms of quasimolecular (QMO) orbitals localized on a hexagon. The strongest Ir-Ir hopping is between 5*d* t_{2g} orbitals of neighboring iridium ions via common oxygens. In this case, an electron on a given Ir t_{2g} orbital propagates around an Ir_6 hexagon with the peculiarity than only a certain t_{2g} orbital at each Ir participates in the hopping,[17] e.g., Ir1(xy)-Ir2(xz)-Ir3(yz)-Ir4(xy)-Ir5(xz)-Ir6(yz) (see Fig. 2 of Ref. 5). These QMOs are analogous to the molecular orbitals of the benzene molecule C_6H_6 except for the fact that in benzene the same p orbital on each carbon ion participates in the formation of the molecular orbital while in Na_2IrO_3, as described above, different t_{2g} orbitals are involved in one QMO and the three t_{2g} orbitals on one Ir ion contribute to three different neighboring QMOs. We elaborate the details of the construction of the QMOs in what follows.

QMO projectors $P_{\mathcal{M}\nu}(\mathbf{k})$ are obtained as linear combinations of Ir t_{2g} projectors $P_{M\nu}(\mathbf{k})$:

$$P_{\mathcal{M}\nu}(\mathbf{k}) = \sum_{M} U_{\mathcal{M},M}T_M(\mathbf{k})P_{M\nu}(\mathbf{k}), \tag{4}$$

where in the Ir t_{2g} projectors $P_{M\nu}(\mathbf{k})$, the index M combines now the atomic index α and orbital index m; i.e., M runs over all t_{2g} orbitals of all equivalent Ir atoms. With QMOs ordered as $\mathcal{M} = A_{1g},E_{2u},E_{1g},B_{1u},E_{1g},E_{2u}$, and Ir t_{2g} orbitals ordered as $M = xy^1,xz^1,yz^1,xy^2,xz^2,yz^2$ (the upper index labels Ir atoms), U is given by [$\omega = \exp(i\pi/3)$]

$$U = \begin{pmatrix} 1 & 1 & 1 & 1 & 1 & 1 \\ 1 & \omega^4 & \omega^2 & -1 & \omega & \omega^5 \\ 1 & \omega^2 & \omega^4 & 1 & \omega^2 & \omega^4 \\ 1 & 1 & 1 & -1 & -1 & -1 \\ 1 & \omega^4 & \omega^2 & 1 & \omega^4 & \omega^2 \\ 1 & \omega^2 & \omega^4 & -1 & \omega^5 & \omega \end{pmatrix}, \tag{5}$$

and $T_M(\mathbf{k})$ are the Bloch factors, accounting for the fact that the 6 sites forming a QMO belong to several different unit cells. Actual values for these factors depend on the manner in which a particular band structure code selects the unit cell (see the Appendix for the WIEN2k settings).

IV. NONRELATIVISTIC ELECTRONIC STRUCTURE

In this section we analyze and discuss the Ir-Ir 5*d* t_{2g} tight-binding parameters for Na_2IrO_3 *up to second nearest neighbors*. As mentioned in Sec. II, three structural distortions are present in Na_2IrO_3: orthorhombic distortion, IrO_6 octahedra rotation, and trigonal distortion. Besides, the stacking of the honeycomb planes inherently violates the rhombohedral symmetry even if each plane is ideal. The formation of QMOs relies on the dominance of *intra*hexagon hopping[5] and therefore is sensitive to structural details. Therefore it is important to understand the role of structural distortions in establishing electron hopping paths. This motivates us to study electronic properties of a number of artificially idealized Na_2IrO_3 unit cells where structural distortions of different types are systematically eliminated.[20] Such a procedure has proven very useful[21] in understanding the behavior of Sr_2IrO_4.

We consider four different crystal structures: (i) the experimental crystal structure,[8] S_{exp}, (ii) an artificially idealized Na_2IrO_3 unit cell, S_1, where the orthorhombic distortion has been removed from the experimental crystal structure, (iii) an artificially idealized Na_2IrO_3 unit cell, S_2, where the IrO_6 octahedra rotations have been removed from S_1, and (iv) an artificially idealized Na_2IrO_3 unit cell, S_3, where the trigonal distortion has been removed from S_2. Table I shows a comparison of total (nonmagnetic) DFT energies for the various structures. As is to be expected, the experimental structure is the energetically most stable case. Tight-binding hopping parameters between Ir t_{2g} orbitals up to second nearest

TABLE I. Nonrelativistic total energies obtained within DFT for the experimental, $E_{S_{\rm exp}}$, and the three idealized, S_i ($i = 1,2,3$), Na_2IrO_3 crystal structures. Energy is given per unit cell containing two formula units.

Structure	$S_{\rm exp}$	S_1	S_2	S_3
$E_{S_i} - E_{S_{\rm exp}}$ (mRyd)	0	0.95	78.90	180.01

neighbors calculated for the four structures are given in Table II and schematically represented in Fig. 3. We consider the following rationale for labeling of the hopping parameters Eq. (3). In the experimental structure of Na_2IrO_3 there are two first NN Ir-Ir distances and two second NN Ir-Ir distances due to the fact that the Ir_6 hexagons are not perfect. We denote the corresponding Ir t_{2g} - Ir t_{2g} hopping parameters as t_1 and $t_{\bar{1}}$ for the first NN and, respectively, t_2 and $t_{\bar{2}}$ for the second NN hoppings. Further, we have various possible hoppings between equal and different t_{2g} orbitals. Regarding first NN, we denote $t_{1\,\rm O}$ and $t_{\bar{1}\,\rm O}$ the hoppings between unlike t_{2g} orbitals via O p states [Fig. 3(a)]. $t_{1\sigma}$ and $t_{\bar{1}\sigma}$ denote NN direct hoppings of σ type. $t_{1\parallel}$ and $t_{\bar{1}\parallel}$ denote NN hoppings between like orbitals lying in parallel planes. In the ideal structure such hoppings consist of linear combinations with equal weight of $dd\pi$ and $dd\delta$ bonds. $t_{1\perp}$ and $t_{\bar{1}\perp}$ denote NN hoppings between unlike orbitals lying in perpendicular planes [see Figs. 3(b) and 3(c)].

Regarding the second NN hopping parameters, $t_{2\,\rm O}$ and $t_{\bar{2}\,\rm O}$ denote hoppings between unlike orbitals via O p and Na s states [Fig. 3(e)]. t_{2a} and t_{2b} ($t_{\bar{2}a}$ and $t_{\bar{2}b}$) denote hoppings between like orbitals as shown in Fig. 3(d) and t_{2c}, t_{2d}, and t_{2e} ($t_{\bar{2}c}$, $t_{\bar{2}d}$, and $t_{\bar{2}e}$) denote hoppings between unlike orbitals [Fig. 3(e)].

A. Experimental crystal structure

Previous electronic structure calculations[5] have identified the dominant hopping integrals for Na_2IrO_3 to be $t_{1\,\rm O}$ and $t_{2\,\rm O}$ [as well as $t_{\bar{1}\,\rm O}$ and $t_{\bar{2}\,\rm O}$; further on, if not explicitly stated otherwise, we refer to both equivalent t_1 (t_2) and $t_{\bar{1}}$ ($t_{\bar{2}}$) when writing t_1 (t_2)]. In Table II column $S_{\rm exp}$ we present the complete list of hopping parameters up to the second nearest neighbors. A TB model based only on these hopping integrals provides

TABLE II. Nearest neighbor (NN) and second NN hopping integrals in meV between Ir t_{2g} orbitals for the experimental structure and three idealized structures S_1, S_2, S_3 of Na_2IrO_3 (see text and Appendix for a description of the structures and parameter labeling). The NN = 0 data are Ir t_{2g} on-site energies and *inter*orbital hoppings; the NN = 1 and NN = $\bar{1}$ (NN = 2 and NN = $\bar{2}$) data are hoppings over nonequivalent (due to orthorhombic distortion) NN (second NN) Ir bonds.

NN		$S_{\rm exp}$	S_1	S_2	S_3
0	$xy \to xy$	−448.8	−422.9	−422.8	−601.1
	$xz \to xz$	−421.5	−421.8	−421.2	−601.1
	$yz \to yz$	−421.5	−421.8	−421.2	−601.1
	$xy \to xz, xy \to yz$	−27.8	−26.4	−21.2	−13.5
	$xz \to yz$	−23.1	−25.2	−18.8	−14.7
1	$xy \to xy$ ($t_{1\parallel}$)	47.7	34.1	27.8	120.8
	$xy \to xz, xy \to yz$ ($t_{1\,\rm O}$)	269.6	268.5	231.7	209.7
	$xy \to xz, xy \to yz$ ($t_{1\perp}$)	−25.6	−16.6	43.7	−5.3
	$xz \to xz, yz \to yz$ ($t_{1\parallel}$)	30.0	33.2	17.2	118.9
	$xz \to xz, yz \to yz$ ($t_{1\sigma}$)	−20.7	3.5	−66.5	−381.6
	$xz \to yz$ ($t_{1\perp}$)	−21.4	−16.4	41.7	−4.9
$\bar{1}$	$xy \to xy$ ($t_{\bar{1}\sigma}$)	25.4	0.2	−65.5	−382.8
	$xy \to xz, xy \to yz$ ($t_{\bar{1}\perp}$)	−11.9	−17.6	46.9	−5.3
	$xz \to xz, yz \to yz$ ($t_{\bar{1}\parallel}$)	33.1	33.9	21.2	120.5
	$xz \to yz$ ($t_{\bar{1}\,\rm O}$)	264.4	264.8	228.7	211.7
2	$xy \to xy$ (t_{2a})	−3.5	−2.6	−18.9	2.0
	$xy \to xz, xy \to yz$ ($t_{2\,\rm O}$)	−75.8	−77.4	−94.7	−82.1
	$xy \to xz, xy \to yz$ (t_{2c})	−36.5	−35.3	−52.1	−38.5
	$xy \to xz, xy \to yz$(t_{2d})	12.5	10.1	1.7	6.9
	$xy \to xz, xy \to yz$ (t_{2e})	−21.4	−19.2	−7.3	1.9
	$xz \to xz, yz \to yz$(t_{2a})	−0.6	−3.1	−16.6	1.4
	$xz \to xz, yz \to yz$ (t_{2b})	−1.5	−1.6	−1.0	5.7
	$xz \to yz$ (t_{2e})	−18.6	−19.0	−7.1	2.4
	$xz \to yz$ (t_{2d})	10.2	10.2	2.4	6.6
$\bar{2}$	$xy \to xy$ ($t_{\bar{2}b}$)	−1.4	−1.4	−1.2	5.7
	$xy \to xz, xy \to yz$ ($t_{\bar{2}e}$)	−19.0	−19.2	−8.4	2.1
	$xy \to xz, xy \to yz$ ($t_{\bar{2}d}$)	9.3	10.2	0.7	7.5
	$xz \to xz, yz \to yz$ ($t_{\bar{2}a}$)	−1.4	−3.0	−17.7	1.5
	$xz \to yz$ ($t_{\bar{2}\,\rm O}$)	−77.0	−78.0	−95.2	−81.9
	$xz \to yz$ ($t_{\bar{2}c}$)	−30.4	−35.1	−51.6	−38.9

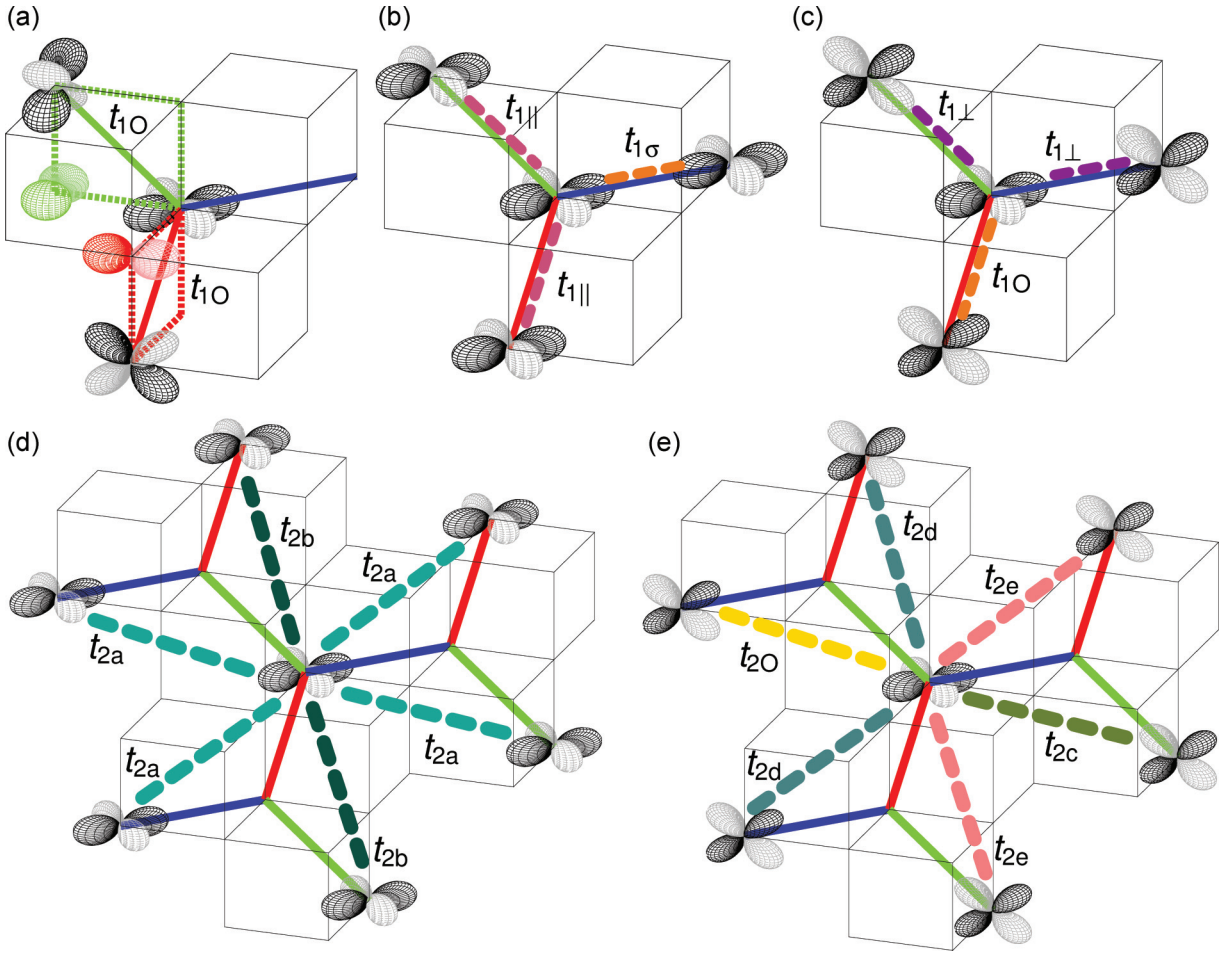

FIG. 3. (Color online) Schematic representation of Ir-Ir t_{2g} hopping paths up to second nearest neighbor in Na_2IrO_3.

already a reasonable description of Na_2IrO_3 Ir t_{2g} states near the Fermi level E_F [Fig. 4(a)].

We first note a very good agreement between the t_{1O} ($\sim$270 meV) and t_{2O} (~-75 meV) values obtained with our WIEN2k-based projection method and with the FPLO code[18] as was used in Ref. 5. These leading Ir t_{2g} hoppings strongly tend to confine the electron's motion to a single Ir hexagon and, as a result, the electronic structure of Na_2IrO_3 near the Fermi level is dominated by the formation of well separated and relatively weakly dispersive QMOs.[5] On an Ir hexagon, as shown above, each Ir atom participates with one of its t_{2g} orbitals (see Fig. 2 of Ref. 5). These orbitals combine to form six QMOs according to the unitary transformation Eq. (5). In support of this picture, Fig. 5(a) shows the density of states of Na_2IrO_3 projected onto the six QMOs (singlets A_{1g} and B_{1u} and doublets E_{2u} and E_{1g}), where states with certain predominant QMO character are clearly separated in energy from one another. The near degeneracy of A_{1g} and E_{2u} states around E_F is rather accidental resulting from the $t_{1O}/t_{2O} \sim -3.6$ ratio (see Table II and Ref. 5). The real-space representations of the QMO Wannier functions onto which the Na_2IrO_3 DOS is being projected are shown in Fig. 6. The QMO Wannier functions were constructed as described in Sec. II by explicitly accounting for the location of each Ir t_{2g} orbital in the crystal.[19]

Other NN and second NN hopping processes involving intraorbital and interorbital hoppings (see Table II) allow an electron to jump from one QMO to another and hence are responsible for the band dispersion. Many of those hoppings are of the same order of magnitude (although mostly by at least an order of magnitude smaller) than t_{2O}, such as $t_{1\|}$ and $t_{\bar{1}\|}$. For the "z" bond such hoppings will be between xz and xz or yz and yz orbitals [see Fig. 3(b)]. These hoppings are equal to 47.7, 30.0, and 33.1 meV, depending on the NN bond (see Table II). In fact, such appreciable variations in magnitude, which violate the D_{6h} symmetry of an ideal Ir hexagon, are ubiquitous among the hoppings that connect neighboring QMOs. Some of them even change sign, such as $t_{1\sigma}$ and $t_{\bar{1}\sigma}$. This feature results from the orthorhombic stacking, distortions within the Ir_2Na planes, and rotations of IrO_6 octahedra.

B. Structure S_1 obtained by removing the orthorhombic distortion

We now consider an idealized Na_2IrO_3 structure without the orthorhombic distortion of Ir hexagons; this structure, which we call S_1, as well as other structures in this section, is tabulated in the Appendix. In the structure S_1, (i) all *intra*layer Ir-Ir bonds are of the same length, i.e., the D_{6h} symmetry of an Ir hexagon is restored, (ii) all NN Ir-O bonds are of

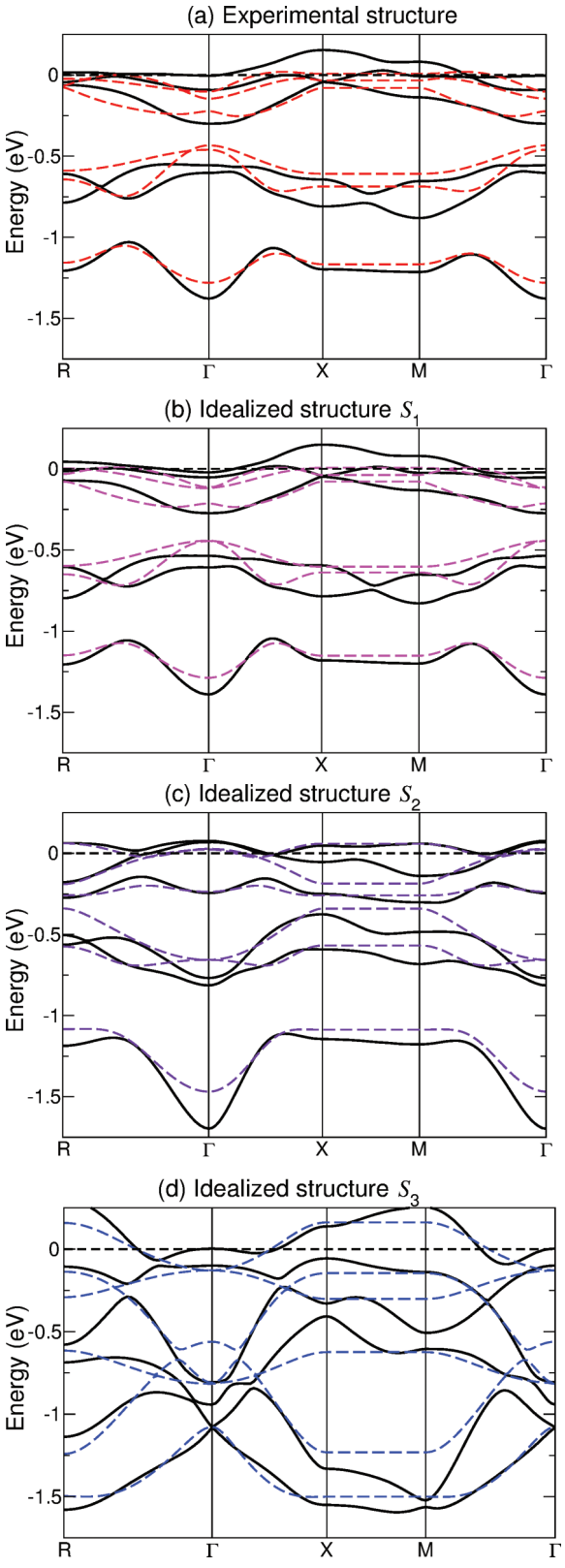

FIG. 4. (Color online) Na_2IrO_3 band structures near the Fermi level $E_F = 0$ calculated using DFT (black solid lines) and a TB model that considers *only* up to NNN hopping processes between Ir t_{2g} orbitals (dashed lines). The data are obtained with (a) experimental crystal structure and idealized structures (b) S_1, (c) S_2, and (d) S_3.

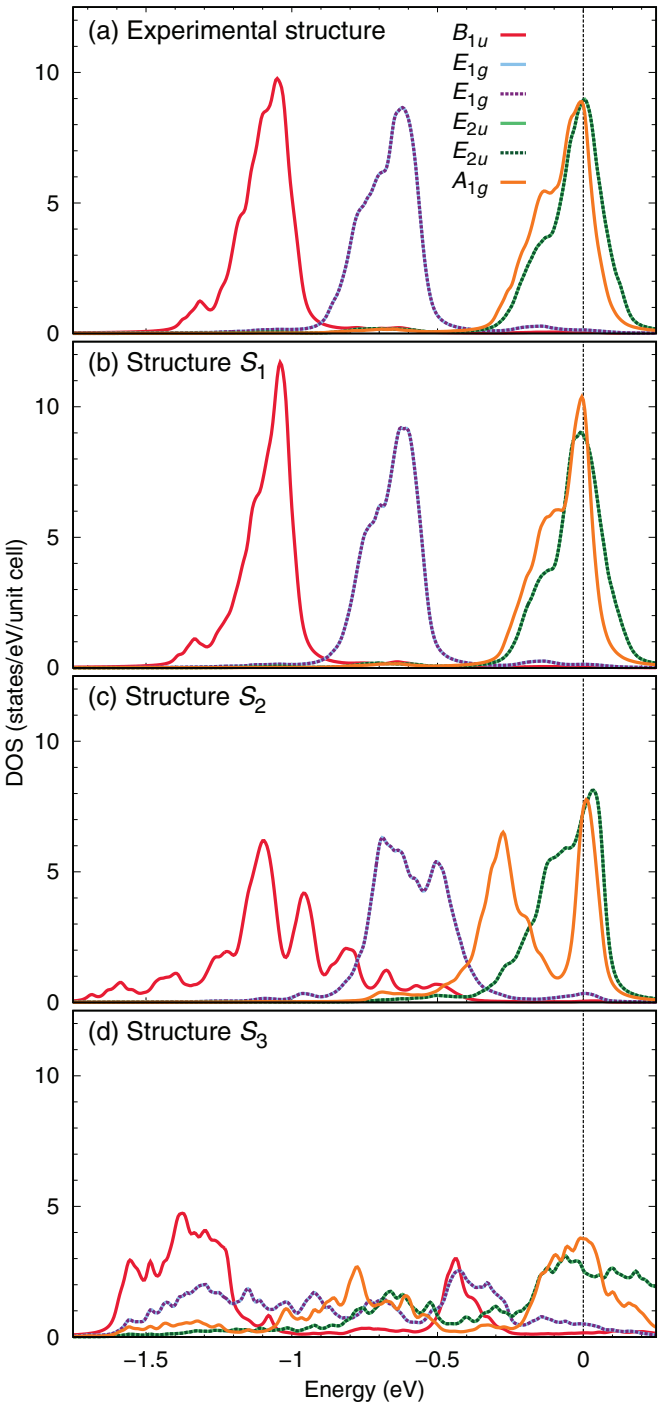

FIG. 5. (Color online) Na_2IrO_3 DOS projected onto QMOs for (a) experimental crystal structure and idealized structures (b) S_1, (c) S_2, and (d) S_3. The Fermi level is set to zero.

the same length, (iii) all Ir-O-Ir bond angles are equal to 98.7°, and (iv) the oxygens lie on the faces of a cube drawn around an Ir hexagon (see Fig. 2 of Ref. 5). The 3D crystal structure, though, remains orthorhombic in this approximation, due to the presence of multiple Ir layers. This explains small residual variations among the nominally equivalent TB model parameters (Table II, column S_1)—for example, comparing parameters labeled with and without an overbar; also, on-site energies like the xy on-site energy are slightly lower than the

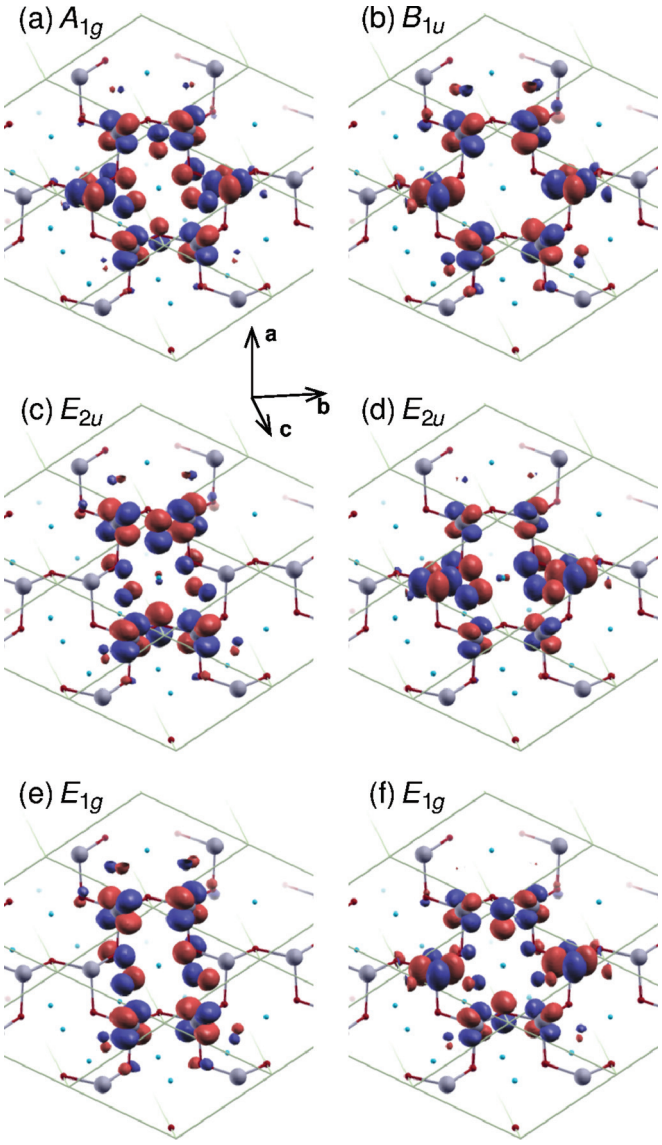

FIG. 6. (Color online) Real-space representation of the QMOs in Na_2IrO_3 obtained by the Wannier projector method.

xz/yz on-site energy. However, these variations of t_{2g} orbital on-site energies, as well as of equivalent hopping integrals, are now noticeably smaller than in the experimental Na_2IrO_3 structure.

We conclude that removal of the orthorhombic distortion restores (to a certain degree) the degeneracy of the Ir t_{2g} orbitals, but does not change the hierarchy of hopping integrals. In the structure S_1, the t_{1O} and t_{2O} values are close to the respective values in the experimental Na_2IrO_3 structure and, as a consequence, the overall structure of the t_{2g} bands is only slightly changed [Figs. 4(b) and 5(b)].

C. Structure S_2 obtained by removing the IrO_6 octahedra rotations

In the structure S_1 that we designed in the previous section, two types of distortions are still present: (i) trigonal squeezing of IrO_6 octahedra along the (111) direction perpendicular to Ir hexagon planes and (ii) IrO_6 octahedra rotations that place O atoms on the cube's faces. We now consider structure S_2, where the IrO_6 octahedra rotations are removed from S_1. In this structure, the Na-O and Ir-O bond lengths are the same (in the experimental structure, the former is considerably longer). This feature enhances the second NN hopping processes through Na s states, such as t_{2O}, t_{2a}, t_{2c} (and the equivalent overbar hoppings) as shown in Table II, column S_2. At the same time, the NN O-assisted hopping t_{1O} gets reduced and the t_{1O}/t_{2O} ratio decreases to ~ -2.4, resulting in a larger separation of the lowest (B_{1u}) band from the rest of t_{2g} bands [Fig. 4(c)]. Formation of QMOs still takes place in structure S_2 [Fig. 5(c)], but the QMO bands are more dispersive compared to the experimental or S_1 structures, due to increased *inter*hexagon NN hopping integrals $t_{1\sigma}$, $t_{1\perp}$ (and equivalent $t_{\bar{1}\sigma}$, $t_{\bar{1}\perp}$); thus, one observes broadening of the A_{1g} band and redistribution of weight away from the E_{2u} doublet.

D. Structure S_3 obtained by removing the trigonal distortion

We finally consider a most idealized Na_2IrO_3 structure S_3 without the trigonal distortion, i.e., with 90° Ir-O-Ir bond angles. Importantly, one can only remove this distortion, while keeping the Ir-O bond length the same, if the Ir-Ir bonds are shortened. Because of that, the hierarchy of hopping integrals changes drastically (Table II, column S_3). The dominant hopping is now the direct NN hopping between like orbitals $t_{1\sigma}$ (and the equivalent $t_{\bar{1}\sigma}$) reaching ~ -380 meV, while the O-assisted hopping t_{1O} ($t_{\bar{1}O}$) has been reduced to ~ 210 meV. Accordingly, the large *inter*hexagon interaction destroys the QMO picture, as illustrated by the strongly dispersive t_{2g} manifold in Fig. 4(d) and the delocalization of individual QMO characters over the whole DOS range in Fig. 5(d). We also observe that the main reason for the trigonal squeeze is the geometrical effect of optimizing simultaneously the Ir-Ir and Ir-O bonds. As a result, even though the on-site t_{2g} orbitals split into an a_{1g} singlet and an e_g doublet, this is not a strong effect and not the driving force for the squeeze, as is often assumed in the spirit of localized limit and the Jahn-Teller effect.

Summarizing these results, in the S_3 structure, the NN direct hopping increases by an order of magnitude compared to the experimental Na_2IrO_3 structure and the NN O-assisted hoppings get suppressed. Therefore we conclude that structural distortions of all types in Na_2IrO_3 act constructively to enhance the *intra*hexagon effective hopping parameters (such as t_{1O} and t_{2O}) and suppress the *inter*hexagon ones (such as NN direct hopping) favoring the formation of QMOs.

V. SPIN-ORBIT COUPLING

We proceed now with the analysis of the electronic structure of Na_2IrO_3 in the presence of spin-orbit (SO) coupling. Previous relativistic DFT calculations[22] showed that Na_2IrO_3 states near the Fermi level experience strong relativistic splitting with pronounced concentration of $j_{\text{eff}} = \frac{1}{2}$ character in the upper two bands. However, the Na_2IrO_3 relativistic states seem to preserve their QMO identity as well [see Fig. S6(b) of Ref. 5]. In order to understand such duality, we set up a TB model for the Ir t_{2g} orbitals that includes also local SO

interaction terms. With this TB + SO model, we are able not only to confirm the relativistic DFT results by calculating DOS but also to access the composition of individual states and trace their evolution as a function of the spin-orbit coupling λ.

A. TB + SO model

We start with a TB model that perfectly describes the nonrelativistic DFT Ir t_{2g} bands of Na_2IrO_3. It includes 321 hopping integrals between up to 50 nearest neighbors. We then double the dimension of the TB Hamiltonian matrix to introduce spin dependence and add local SO coupling terms $\langle \lambda \mathbf{L}\cdot\mathbf{S}\rangle$ that mix spin-$\uparrow$ and spin-$\downarrow$ subspaces:

	$xy\uparrow$	$xz\uparrow$	$yz\uparrow$	$xy\downarrow$	$xz\downarrow$	$yz\downarrow$
$xy\uparrow$	0	0	0	0	$\frac{\lambda}{2}$	$-\frac{i\lambda}{2}$
$xz\uparrow$	0	0	$\frac{i\lambda}{2}$	$-\frac{\lambda}{2}$	0	0
$yz\uparrow$	0	$-\frac{i\lambda}{2}$	0	$\frac{i\lambda}{2}$	0	0
$xy\downarrow$	0	$-\frac{\lambda}{2}$	$-\frac{i\lambda}{2}$	0	0	0
$xz\downarrow$	$\frac{\lambda}{2}$	0	0	0	0	$-\frac{i\lambda}{2}$
$yz\downarrow$	$\frac{i\lambda}{2}$	0	0	0	$\frac{i\lambda}{2}$	0

(6)

Importantly, even though SO coupling is a local on-site interaction, it couples neighboring quasimolecular orbitals and therefore is **k**-vector dependent in the QMO basis.

Having thus set up the TB model, we vary the SO coupling strength λ until the best matching with the DFT relativistic bands is achieved, which is found to correspond to $\lambda = 0.44$ eV (Fig. 7).

Since our purpose is to reconcile the QMO and relativistic orbital (RO) pictures, we analyze the $\lambda\mathbf{L}\cdot\mathbf{S}$ matrix elements between spin-$\uparrow$ and spin-$\downarrow$ QMOs to see how SO coupling mixes QMO characters. They can be easily obtained by applying the unitary transformation $UT(\mathbf{k})$ [Eq. (5)] to the $\lambda\mathbf{L}\cdot\mathbf{S}$ matrix in the t_{2g} basis:

$$H^{\mathrm{SO}}_{\mathrm{QMO}}(\mathbf{k}) = UT(\mathbf{k})H^{\mathrm{SO}}_{t_{2g}}T^{H}(\mathbf{k})U^{H}. \tag{7}$$

This equation explicitly illustrates how **k**-vector dependence enters the SO matrix elements in the QMO basis. Concise expressions can be derived if one notes that QMOs can be represented by their "winding number" n which defines a phase change $\Delta\phi = \frac{n\pi}{3}$ of t_{2g} orbitals around a hexagon. In this notation, QMOs $A_{1g}, E_{2u}, E_{1g}, B_{1u}, E_{1g}, E_{2u}$ correspond to, respectively, $n = 0,1,2,3,4,5$ winding numbers. The $\lambda\mathbf{L}\cdot\mathbf{S}$ matrix elements in the QMO basis are given then by

$$\begin{aligned} H^{\mathrm{SO}}_{n\uparrow n'\uparrow} = {} & \frac{\lambda}{2} i \exp\frac{(n'-n)\pi i}{2} \cos\frac{(n'-n)\pi}{2} \cos(k_x + k_y) \\ & \times \left(\exp\frac{2(2n'-n)\pi i}{3} - \exp\left[-\frac{2(2n-n')\pi i}{3} \right] \right) \\ & + \frac{\lambda}{2} i \exp\frac{(n'-n)\pi i}{2} \sin\frac{(n'-n)\pi}{2} \sin(k_x + k_y) \\ & \times \left(\exp\frac{2(2n'-n)\pi i}{3} + \exp\left[-\frac{2(2n-n')\pi i}{3} \right] \right) \end{aligned} \tag{8}$$

and

$$\begin{aligned} H^{\mathrm{SO}}_{n\uparrow n'\downarrow} = {} & 2 \exp\frac{(n'-n)\pi i}{2} \\ & \times \left[\exp\frac{4n'\pi i}{3} \cos\left(-\frac{(n'-n)\pi}{2} + k_y \right) \right. \\ & - \exp\left(-\frac{4n\pi i}{3} \right) \cos\left(-\frac{(n'-n)\pi}{2} - k_y \right) \\ & + i \exp\frac{2n'\pi i}{3} \cos\left(-\frac{(n'-n)\pi}{2} - k_x \right) \\ & \left. - i \exp\left(-\frac{2n\pi i}{3} \right) \cos\left(-\frac{(n'-n)\pi}{2} + k_x \right) \right]. \end{aligned} \tag{9}$$

We list numerical values of the matrix elements for two representative **k** vectors: $\mathbf{k} = (0,0,0)$ (point Γ) (first two tables) and $\mathbf{k} = (\frac{\pi}{2},0,0)$ (last two tables):

	$n=5$ $E_{2u}\uparrow$	$n=0$ $A_{1g}\uparrow$	$n=1$ $E_{2u}\uparrow$	$n=2$ $E_{1g}\uparrow$	$n=3$ $B_{1u}\uparrow$	$n=4$ $E_{1g}\uparrow$
$E_{2u}\uparrow$	C_1	0	0	0	$-C_1$	0
$A_{1g}\uparrow$	0	0	0	$-C_1$	0	C_1
$E_{2u}\uparrow$	0	0	$-C_1$	0	C_1	0
$E_{1g}\uparrow$	0	$-C_1$	0	C_1	0	0
$B_{1u}\uparrow$	$-C_1$	0	C_1	0	0	0
$E_{1g}\uparrow$	0	C_1	0	0	0	$-C_1$

(10)

	$n=5$ $E_{2u}\downarrow$	$n=0$ $A_{1g}\downarrow$	$n=1$ $E_{2u}\downarrow$	$n=2$ $E_{1g}\downarrow$	$n=3$ $B_{1u}\downarrow$	$n=4$ $E_{1g}\downarrow$
$E_{2u}\uparrow$	C_2	0	0	0	C_4	0
$A_{1g}\uparrow$	0	0	0	$-C_3$	0	$-C_4$
$E_{2u}\uparrow$	0	0	$-C_2$	0	C_3	0
$E_{1g}\uparrow$	0	C_4	0	C_2	0	0
$B_{1u}\uparrow$	$-C_3$	0	$-C_4$	0	0	0
$E_{1g}\uparrow$	0	C_3	0	0	0	$-C_2$

(11)

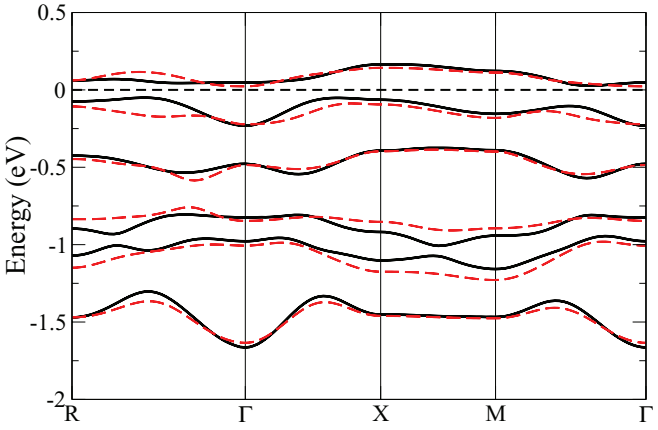

FIG. 7. (Color online) WIEN2k relativistic band structure (black solid lines) versus TB + SO model relativistic band structure (red dashed lines) of Na_2IrO_3 as described in the text. In model calculations, $\lambda = 0.44$ eV was used.

	$n=5$	$n=0$	$n=1$	$n=2$	$n=3$	$n=4$
	$E_{2u}\uparrow$	$A_{1g}\uparrow$	$E_{2u}\uparrow$	$E_{1g}\uparrow$	$B_{1u}\uparrow$	$E_{1g}\uparrow$
$E_{2u}\uparrow$	$\frac{\lambda}{6}$	0	$\frac{\lambda}{6}$	0	$-\frac{\lambda}{3}$	0
$A_{1g}\uparrow$	0	$\frac{\lambda}{6}$	0	$-\frac{\lambda}{3}$	0	$\frac{\lambda}{6}$
$E_{2u}\uparrow$	$\frac{\lambda}{6}$	0	$-\frac{\lambda}{3}$	0	$\frac{\lambda}{6}$	0
$E_{1g}\uparrow$	0	$-\frac{\lambda}{3}$	0	$\frac{\lambda}{6}$	0	$\frac{\lambda}{6}$
$B_{1u}\uparrow$	$-\frac{\lambda}{3}$	0	$\frac{\lambda}{6}$	0	$\frac{\lambda}{6}$	0
$E_{1g}\uparrow$	0	$\frac{\lambda}{6}$	0	$\frac{\lambda}{6}$	0	$-\frac{\lambda}{3}$

(12)

	$n=5$	$n=0$	$n=1$	$n=2$	$n=3$	$n=4$
	$E_{2u}\downarrow$	$A_{1g}\downarrow$	$E_{2u}\downarrow$	$E_{1g}\downarrow$	$B_{1u}\downarrow$	$E_{1g}\downarrow$
$E_{2u}\uparrow$	$C_1 i$	C_5	0	$-\frac{\lambda}{6}$	C_6	C_7
$A_{1g}\uparrow$	C_5^*	0	C_5	$-C_6^*$	$\frac{\lambda}{3}$	$-C_6$
$E_{2u}\uparrow$	0	C_5^*	$-C_1 i$	C_7^*	C_6^*	$-\frac{\lambda}{6}$
$E_{1g}\uparrow$	$-\frac{\lambda}{6}$	C_6	C_7	$C_1 i$	C_5	0
$B_{1u}\uparrow$	$-C_6^*$	$\frac{\lambda}{3}$	$-C_6$	C_5^*	0	C_5
$E_{1g}\uparrow$	C_7^*	C_6^*	$-\frac{\lambda}{6}$	0	C_5^*	$-C_1 i$

(13)

with $C_1 = \frac{\lambda}{\sqrt{12}}$, $C_2 = \frac{\lambda}{\sqrt{12}}(1+i)$, $C_3 = 0.105663\lambda(1+i)$, $C_4 = 0.394337\lambda(1+i)$, $C_5 = \frac{\lambda}{12} + \frac{\lambda}{2\sqrt{12}}i$, $C_6 = \frac{\lambda}{4} + \frac{\lambda}{2\sqrt{12}}i$, $C_7 = -\frac{\lambda}{6} + \frac{\lambda}{\sqrt{12}}i$.

Several comments are in place here. First, spin-orbit coupling mixes QMOs at all **k** vectors. Even at the Γ point, i.e., on the same hexagon, the three upper QMOs (A_{1g} and two E_{2u}) are SO coupled to the three lower QMOs (B_{1u} and two E_{1g}), which explains sizable shifts of the relativistic bands compared to the nonrelativistic ones at this **k** vector. Additionally, SO coupling induces splitting of the degenerate E_{2u} and E_{1g} states at all **k** vectors. Another striking feature of the calculated $\lambda\mathbf{L}\cdot\mathbf{S}$ matrix is that its A_{1g}, E_{2u} (upper triplet) and B_{1u}, E_{1g} (lower triplet) blocks are identical. This means that if not for the accidental near degeneracy of the A_{1g} and E_{2u} states (which magnifies the SO-induced energy shifts) the upper and the lower triplets would have been equally affected by the SO coupling.

B. Quasimolecular orbital basis versus relativistic basis

The main difficulty in describing the Na_2IrO_3 band structure is that it interpolates between eigenstates of two Hamiltonians: the *itinerant* TB Hamiltonian of (primarily) *intra*hexagon electron hopping that preserves the s_z spin subspace and the *local* spin-orbit (SO) interaction $\lambda\mathbf{L}\cdot\mathbf{S}$ Hamiltonian that couples *different* spin subspaces. The eigenstates of the TB Hamiltonian are quasimolecular orbitals (QMOs), while the eigenstates of the SO interaction (in the t_{2g} subspace) are *relativistic orbitals* (ROs) $|j_{\rm eff}, j_{\rm eff}^z\rangle$ characterized by an effective total angular momentum $j_{\rm eff}$ and its z projection $j_{\rm eff}^z$:

$$\left|\frac{1}{2},\frac{1}{2}\right\rangle = \frac{1}{\sqrt{3}}|xy\uparrow\rangle + \frac{i}{\sqrt{3}}|xz\downarrow\rangle + \frac{1}{\sqrt{3}}|yz\downarrow\rangle,$$
$$\left|\frac{1}{2},-\frac{1}{2}\right\rangle = \frac{i}{\sqrt{3}}|xz\uparrow\rangle - \frac{1}{\sqrt{3}}|yz\uparrow\rangle + \frac{1}{\sqrt{3}}|xy\downarrow\rangle,$$
$$\left|\frac{3}{2},\frac{3}{2}\right\rangle = \frac{i}{\sqrt{2}}|xz\uparrow\rangle + \frac{1}{\sqrt{2}}|yz\uparrow\rangle,$$
$$\left|\frac{3}{2},\frac{1}{2}\right\rangle = -\sqrt{\frac{2}{3}}|xy\uparrow\rangle + \frac{i}{\sqrt{6}}|xz\downarrow\rangle + \frac{1}{\sqrt{6}}|yz\downarrow\rangle,$$
$$\left|\frac{3}{2},-\frac{1}{2}\right\rangle = \frac{i}{\sqrt{6}}|xz\uparrow\rangle - \frac{1}{\sqrt{6}}|yz\uparrow\rangle - \sqrt{\frac{2}{3}}|xy\downarrow\rangle,$$
$$\left|\frac{3}{2},-\frac{3}{2}\right\rangle = -\frac{i}{\sqrt{2}}|xz\downarrow\rangle + \frac{1}{\sqrt{2}}|yz\downarrow\rangle.$$

(14)

This basis[23] can be explained as follows: Three t_{2g} orbitals (total degeneracy, including spins, is 6) are split into a lower lying quartet $j_{\rm eff} = 3/2$ and an upper lying $j_{\rm eff} = 1/2$ doublet, and the $5d$ electrons of Ir^{4+} fully occupy the lower quartet leaving the upper $j_{\rm eff} = 1/2$ doublet half filled. This makes this situation similar to a nondegenerate Hubbard model ($S = 1/2$ doublet on a site), with the important difference that in the Hubbard model the hopping matrix elements preserve the s_z spin subspace, while here the states of the $j_{\rm eff} = 1/2$ doublet are spin-orbit mixed states, leading to a strong anisotropy of hoppings and their dependence on spin (or rather total moment) direction. This may bring about anisotropic exchange, e.g., the Kitaev exchange on a honeycomb lattice.[2]

By gradually increasing an effective spin-orbit coupling strength $\lambda_{\rm eff}$,

$$\lambda_{\rm eff} = \frac{\lambda^2}{(t_{1\rm O})^2 + \lambda^2}, \quad t_{1\rm O} = 0.270\ \text{eV}, \tag{15}$$

from 0 to 1, one can trace a smooth evolution of the TB + SO model eigenvalues from, respectively, the nonrelativistic (QMO) limit to the fully relativistic (RO) limit [see Fig. 8(a) for the data at the Γ point]. An SO coupling parameter of $\lambda = 0.44$ eV for Na_2IrO_3 corresponds to $\lambda_{\rm eff} = 0.73$, which is marked by a vertical dotted line in Fig. 8.

The RO basis is an attractive starting point to describe the low-energy physics of Na_2IrO_3 as it allows us to truncate the Hamiltonian to only $j_{\rm eff} = \frac{1}{2}$ states that dominate near the Fermi energy and map Na_2IrO_3 onto the Kitaev-Heisenberg model. Although this approach might seem reasonable given the noticeable separation of the $j_{\rm eff} = \frac{1}{2}$ and $j_{\rm eff} = \frac{3}{2}$ characters in the DOS of Na_2IrO_3 [cf. Fig. 2(b) of Ref. 22], we argue that the itinerant terms are too strong to be neglected (which should not be surprising since $\lambda = 0.44$ eV $< W \approx 4t_{1\rm O} = 1$ eV) and that, consequently, the QMO basis is as well (or as poorly) justified to work with as the RO basis.

To support this statement, let us concentrate on the TB + SO model states at the Γ point. Figure 8(a) shows the evolution of the model eigenvalues as a function of $\lambda_{\rm eff}$ [Eq. (15)]. In the nonrelativistic limit ($\lambda_{\rm eff} = 0$), the states are almost purely (with slight deviation due to orthorhombic distortion) QMOs, ordered as $B_{1u}, E_{1g}, A_{1g}, E_{2u}$ with increasing energy.[24] At the same time, at each state the $j_{\rm eff} = \frac{1}{2}$ contribution is 1/3 and the $j_{\rm eff} = \frac{3}{2}$ contribution is, correspondingly, 2/3 (for one of the two Ir atoms). Note that since the model distinguishes spin-↑ and spin-↓ states, each level is doubly degenerate.

With the QMO splitting obviously prevailing for zero SO coupling, we now want to quantify the QMO character rectification upon increasing $\lambda_{\rm eff}$ by calculating the QMO and

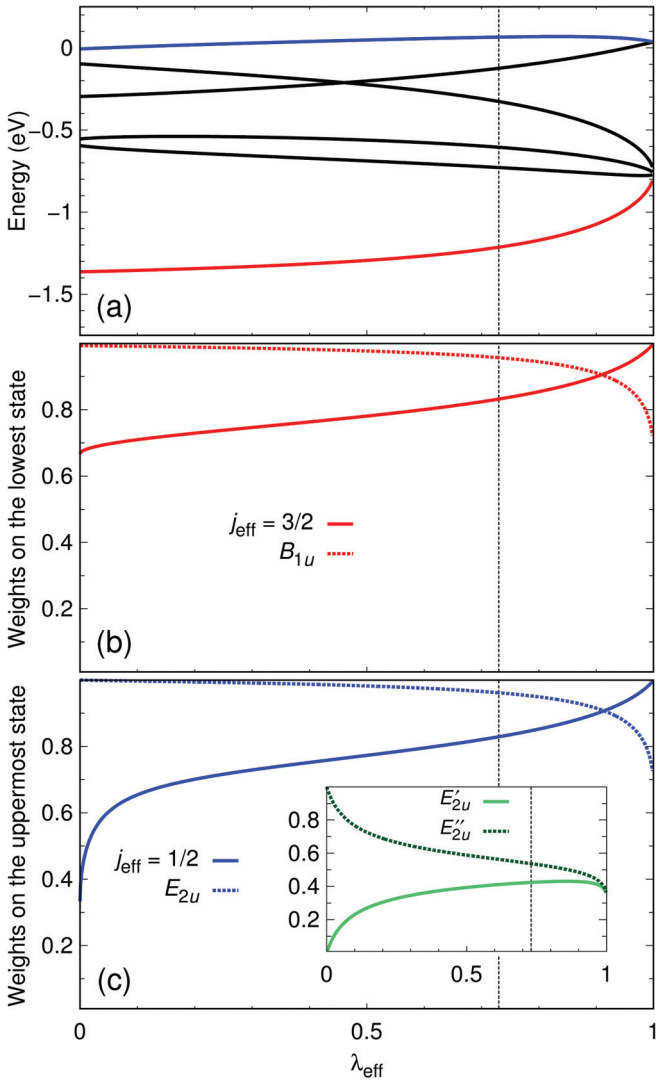

FIG. 8. (Color online) Properties of the TB + SO model of Na_2IrO_3 at the Γ point as a function of effective SO coupling $\lambda_{\rm eff}$ defined in Eq. (15). The vertical dotted line marks the realistic $\lambda_{\rm eff} = 0.73$ value for Na_2IrO_3. (a) The eigenvalues of the TB + SO model at Γ. Eigenenergies have been scaled by $\sqrt{1-\lambda_{\rm eff}}$ to keep them within the [−1.5,0.2] eV range. (b) The $j_{\rm eff} = \frac{3}{2}$ (solid line) and B_{1u} (dashed line) weights on the lowest state. (c) The $j_{\rm eff} = \frac{1}{2}$ (solid line) and total E_{2u} (dashed line) weights on the uppermost state. Inset shows individual contributions from the two E_{2u} QMOs.

RO weights on two selected states: the lowest (B_{1u}) and the uppermost (E_{2u}). The B_{1u} state [Fig. 8(b)] is a simpler case as it is nondegenerate (apart from spin) and quite well separated from the rest of the QMOs so that the SO effects here should be less important. Changing $\lambda_{\rm eff}$ from 0 to 0.73 (Na_2IrO_3 value), the $j_{\rm eff} = \frac{3}{2}$ weight on this state increases from 0.6667 to 0.8320, whereas the B_{1u} weight is only slightly reduced from 0.9932 to 0.9567. This indicates that the lowest relativistic state at the Γ point in Na_2IrO_3 is better described by a QMO B_{1u} than by one of the $j_{\rm eff} = \frac{3}{2}$ ROs. In fact, this turns out to hold for the whole lowest relativistic band [cf. the $j_{\rm eff}$- and QMO-projected Na_2IrO_3 DOS in, respectively, Fig. 2(b) of Ref. 22 and Fig. S6(b) of Ref. 5].

The uppermost state is one of the E_{2u} doublet states. It is near degenerate with A_{1g} and the other E_{2u} and, therefore, the SO effects are here particularly strong. At the Γ point, though, it can only couple to itself or to the other E_{2u} [see Eqs. (10) and (11)], depending on which linear combination of these degenerate states is considered. Upon switching $\lambda_{\rm eff}$ on, the $j_{\rm eff} = \frac{1}{2}$ weight on this upper states rapidly grows from 0.3333 to ∼0.6 in the range $0 < \lambda_{\rm eff} < 0.05$, and then gradually increases to 0.8295 at $\lambda_{\rm eff} = 0.73$ [Fig. 8(c)]. At the same time, the weight of one of the E_{2u} states (we may call it E'_{2u}) is reduced from 1.0 to 0.53730 [see inset of Fig. 8(c)]. However, the total weight of two E_{2u} states is barely changed: At $\lambda_{\rm eff} = 0.73$ it equals 0.9617. This means that the uppermost relativistic state at the Γ point in Na_2IrO_3 is very well described by a linear combination of two E_{2u} states (which is also a QMO) with, in general, $\lambda_{\rm eff}$-dependent individual contributions.

The B_{1u} and E_{2u} states (at $\lambda = 0$) seem to simultaneously bear both RO and QMO features up to very strong SO coupling, with the QMO character dominating for $\lambda_{\rm eff} < 0.9$. This can also be illustrated by inspecting the composition of, e.g., the lowest energy band state as shown in Table III. At zero SO coupling, the doubly degenerate lowest state corresponds to (almost) pure $B_{1u}\uparrow$ and $B_{1u}\downarrow$ QMOs.[25] At $\lambda_{\rm eff} = 0.73$, the structure of this state is strikingly similar to the B_{1u} states, with only slight admixtures of the xz and yz orbitals of opposite spin. Even at some very high $\lambda_{\rm eff}$, when the RO $j_{\rm eff} = \frac{3}{2}$ weight is close to 1, the states retain the $B_{1u}\uparrow$ and $B_{1u}\downarrow$ QMO features.

The features shown in this section, not unexpectedly, characterize Na_2IrO_3 as intermediate between the nonrelativistic (pure quasimolecular orbital) and fully relativistic (pure RO) cases.

Moreover, these results show that in the RO representation, the upper band states are not pure $j_{\rm eff} = 1/2$ states but there is some significant mixing of $j_{\rm eff} = 3/2$ states. In fact, for the upper band states, the projections onto $j_{\rm eff} = 1/2$ and $j_{\rm eff} = 3/2$ are, respectively, 0.64 and 0.21 with $2(0.64^2 + 2 \times 0.21^2) = 1$, while in the nonrelativistic case these projections are both equal to $\sqrt{1/6} = 0.41$. Note that looking at the weights may be misleading. Indeed this state appears to be $2 \times 0.64^2 = 82\%$ pure $j_{\rm eff} = 1/2$ state [Fig. 8 (bottom)], but its *projection* on the $j_{\rm eff} = 3/2$ state is only twice smaller than in the nonrelativistic case. In other words, the hopping between the upper Kramers doublets, initially not considered in Ref. 2, is only reduced by about a factor of two compared to the nonrelativistic case. One but possibly not the only consequence of this fact is that the contribution of the Kitaev term in the analysis below may be overestimated, probably by as much as a factor of two.

C. Comparison with experiment: Branching ratio

An argument frequently used to justify the assumption of pure ROs in Na_2IrO_3 is that it is experimentally supported. However, the experimental evidence is inconclusive. It is first assumed that the electronic states are pure ROs and then it is shown that this assumption does not contradict the experiment, yet the experiments, upon a closer look, do not falsify the DFT picture, either. A typical and, by far, the most often used quantity to discuss the nature of the states in iridates is the branching ratio (BR) extracted from x-ray absorption

TABLE III. Expansion coefficients of the lowest doubly degenerate energy states of the TB + SO model in the t_{2g} basis (the upper index of the t_{2g} orbitals labels Ir atoms in the unit cell). The coefficients are given for three λ ($\lambda_{\rm eff}$) values. The B_{1u} and $j_{\rm eff} = \frac{3}{2}$ weights of the various states are given at the bottom of the table.

	$\lambda = 0$ ($\lambda_{\rm eff} = 0$)		$\lambda = 0.44$ eV ($\lambda_{\rm eff} = 0.73$)		$\lambda = 2.66$ eV ($\lambda_{\rm eff} = 0.99$)	
$xy^1\uparrow$	-0.454	0.0	-0.453	0.0	-0.444	0.0
$xz^1\uparrow$	-0.383	0.0	$-0.363 + 0.056i$	$-0.053 - 0.100i$	$-0.263 + 0.150i$	$-0.142 - 0.200i$
$yz^1\uparrow$	-0.383	0.0	$-0.363 - 0.056i$	$-0.100 - 0.053i$	$-0.263 - 0.150i$	$-0.200 - 0.142i$
$xy^2\uparrow$	0.454	0.0	0.453	0.0	0.444	0.0
$xz^2\uparrow$	0.383	0.0	$0.363 - 0.056i$	$0.053 + 0.100i$	$0.263 - 0.150i$	$0.142 + 0.200i$
$yz^2\uparrow$	0.383	0.0	$0.363 + 0.056i$	$0.100 + 0.053i$	$0.263 + 0.150i$	$0.200 + 0.142i$
$xy^1\downarrow$	0.0	-0.454	0.0	-0.453	0.0	-0.444
$xz^1\downarrow$	0.0	-0.383	$0.053 - 0.100i$	$-0.363 - 0.056i$	$0.142 - 0.200i$	$-0.263 - 0.150i$
$yz^1\downarrow$	0.0	-0.383	$0.100 - 0.053i$	$-0.363 + 0.056i$	$0.200 - 0.142i$	$-0.263 + 0.150i$
$xy^2\downarrow$	0.0	0.454	0.0	0.453	0.0	0.444
$xz^2\downarrow$	0.0	0.383	$-0.053 + 0.100i$	$0.363 + 0.056i$	$-0.142 + 0.200i$	$0.263 + 0.150i$
$yz^2\downarrow$	0.0	0.383	$-0.100 + 0.053i$	$0.363 - 0.056i$	$-0.200 + 0.142i$	$0.263 - 0.150i$
$j_{\rm eff} = \frac{3}{2}$ weight	0.6667		0.8320		0.9816	
B_{1u} weight	0.9932		0.9567		0.7824	

spectroscopy (XAS) experiments. In XAS, essentially, $\langle \mathbf{L}\cdot\mathbf{S}\rangle$ is measured. This expectation value is of course zero without spin-orbit coupling. A detailed and very insightful analysis can be found, for instance, in Refs. 26–29. In particular, it is shown that, for a related iridate, the main contribution to $\langle \mathbf{L}\cdot\mathbf{S}\rangle$ (1.4 out of 2.1) does not come from the t_{2g} orbitals, which define the $j_{\rm eff} = 1/2$ states, but from the admixture of the e_g orbitals. In our calculations—shown below—we observe the same behavior.

We apply our TB + SO model to calculate $\langle \mathbf{L}\cdot\mathbf{S}\rangle$ for Na_2IrO_3 where $\mathbf{L}$ and $\mathbf{S}$ are, respectively, the *total* orbital and spin angular momenta of Ir $5d$ electrons. $\langle \mathbf{L}\cdot\mathbf{S}\rangle$ is related to the experimentally accessible branching ratio as

$$\mathrm{BR} = \frac{(2-r)}{(1+r)}, \quad r = \frac{\langle \mathbf{L}\cdot\mathbf{S}\rangle}{n_{\rm h}}, \tag{16}$$

with $n_{\rm h} = 5$ being the average number of $5d$ Ir holes.[30,31] In recent XAS measurements,[32] BR = 5.5–5.7, translating to $\langle \mathbf{L}\cdot\mathbf{S}\rangle = -2.7\hbar^2$, was obtained for Na_2IrO_3 and interpreted as a sign of strong spin-orbit coupling.

When applying the TB + SO model that we constructed for Na_2IrO_3 in Sec. V A the calculated $\langle \mathbf{L}\cdot\mathbf{S}\rangle = -0.73\hbar^2$ (as compared to $-1\hbar^2$ in the limit $\lambda_{\rm eff} = 1$). This value is several times smaller than the experimental value. This is, however, not unexpected given the significant contribution of the Ir e_g empty states to $\langle \mathbf{L}\cdot\mathbf{S}\rangle$ (cf. Ref. 26), which are not considered in the TB + SO model discussed in the previous section. In order to make a meaningful comparison with experiment, we extend our TB + SO model to include (in the same spirit) also the Ir e_g states. $\langle \mathbf{L}\cdot\mathbf{S}\rangle$ within such a model is $-1.91\hbar^2$. This is about 30% less than the experimental value reported by Clancy *et al.*[32] This result is indeed in good agreement with experiment, given the large fluctuations in experimental values. For instance, Ref. 32 reported $\langle \mathbf{L}\cdot\mathbf{S}\rangle = -3.1\hbar^2$ for Sr_2IrO_4 while Ref. 26 reported $-2.1\hbar^2$ (about 30% difference) for the same compound. This example gives a sense of possible fluctuations between results of different experimental groups, and therefore our theoretical $\langle \mathbf{L}\cdot\mathbf{S}\rangle$ value for Na_2IrO_3 might be even closer to the true result.

The main conclusion from these calculations is that with the TB + SO model based on all *five* Ir $5d$ orbitals we are able to reasonably reproduce the large experimentally measured $\langle \mathbf{L}\cdot\mathbf{S}\rangle$ value in Na_2IrO_3, which validates our approach. As our analysis shows, the large $\langle \mathbf{L}\cdot\mathbf{S}\rangle$ does not necessarily mean an ideal separation of $j_{\rm eff} = \frac{3}{2}$ and $j_{\rm eff} = \frac{1}{2}$ RO states, but rather the effect of e_g states also contributing in the process. Due to the peculiar electron hopping hierarchy in Na_2IrO_3, QMOs might be a better basis.

In conclusion, the XAS experiments only tell us that the upper Kramers doublet has a considerable contribution coming from $j_{\rm eff} = 1/2$, but not that it is a pure RO state.

D. Comparison with experiment: RIXS

Another experiment sometimes quoted as supporting the fully relativistic $j_{\rm eff} = \frac{1}{2}$ picture is resonant inelastic x-ray scattering (RIXS).[33] In this experiment a joint density of electronic states (JDOS) is probed, somewhat similar to that in the infrared absorption but with different matrix elements. The authors of Ref. 33 observed several peaks in JDOS, of which the lowest peak at $\sim$0.42 eV was interpreted as transitions across the Mott-Hubbard gap, consistent with a 30% smaller optical absorption threshold. The next two peaks are close to each other at 0.72 and 0.83 eV and were ascribed to transitions from the $j_{\rm eff} = 3/2$ quartet into the upper $j_{\rm eff} = 1/2$ doublet. The splitting of 110 meV was ascribed to the trigonal splitting. Altogether, this interpretation suggests an SO coupling $\lambda \sim \frac{2}{3}(\frac{0.72+0.83}{2} - \frac{0.42}{2})$ eV ≈ 0.39 eV, a very reasonable number, if slightly too small.

This analysis, even though it looks reasonable on the first glance, has serious shortcomings. First, the deduced trigonal splitting is nearly twice as large as the actual trigonal splitting. In fact, the trigonal splitting is decided by the electrostatic field of the ligands, and in addition one-electron hoppings; both are very well accounted for by the DFT calculations, which give $\Delta_T = 75$ meV. Second, even a $\Delta_T = 110$ meV cannot produce well separated peaks in JDOS, given that the Ir-Ir hopping is $t_{1\rm O} = 270$ meV. Third, even if one completely

neglects the Ir-Ir hoppings,[33] in order to extract λ and Δ_T one has to diagonalize the full Hamiltonian including both factors and then fit the resulting eigenvalues to the observed peaks. After doing that, one gets $\lambda = 0.5$ eV and $\Delta_T = 180$ meV. Although the previous numbers are a rough estimate since they depend on the direction of the Ir spins as well as on U (here we considered $U = 0$), the latter number is more than twice the actual trigonal splitting. This argument shows that an interpretation of RIXS in terms of infinitely narrow bands split by the trigonal field may not be completely correct.

We find, on the other hand, that this experiment is consistent with DFT band structure. To demonstrate that, we have performed DFT calculations for the magnetic zigzag phase. We note that the results do not depend qualitatively on the choice of the pattern and the magnetization direction. In order to account for the missing correlation effects and adjust the direct gap to be consistent with infrared measurements,[11] we applied a rigid shift of 200 meV between the occupied and empty bands ("scissor operator"). This exercise gives a JDOS which has a broad feature, consisting of (i) a peak at 0.42 and a shoulder 0.48 eV (compared to 0.42 eV in the experiment) corresponding to the transition between the top QMOs and (ii) a peak at 0.77 eV and a shoulder at 0.81 eV corresponding to transitions from the lower QMOs. While the experiment finds two peaks at 0.72 and 0.83 eV, one should keep in mind that the matrix elements, omitted in our calculation, can easily suppress or enhance a shoulder, making it disappear (at 0.48 eV) or become a separate peak (at 0.81 eV). Therefore we conclude that the agreement between experiment and our calculations, simplified as they are, is reasonably good.

VI. MAGNETISM

We proceed now with the discussion of the magnetic behavior of Na_2IrO_3. Neutron diffraction experiments reported long-range antiferromagnetic order at low temperatures in a zigzag pattern.[8] This ordering was confirmed by relativistic spin-polarized DFT calculations[5] where we showed that it is the itinerancy of the system that stabilizes the zigzag configuration. Such a pattern was also predicted from the localized nnKH model[2,4] [Eq. (1)]. In the following we will provide *ab initio*–derived estimates for the Kitaev and Heisenberg terms and will show that in the physically reasonable parameter range this model unfortunately fails to reproduce the experimentally observed magnetic order.

A. Nearest neighbor Kitaev-Heisenberg model

One term neglected in the conventional Kitaev-Heisenberg model treatment is the single-site magnetocrystalline anisotropy. Localized electrons with the spin 1/2 do not have any anisotropy, no matter how strong the spin-orbit coupling is. However, if hopping is considered, electrons can have a preferred spin direction, which in the language of the nnKH Hamiltonian would be reflected in a single-site term proportional, in the lowest order, to $(\mathbf{A}\cdot\mathbf{S})^2$ where $\mathbf{A}$ is a vector. Such terms are usually neglected when dealing with the nnKH model. Our calculations[5] without including U show a magnetic anisotropy as large as 3 meV per Ir (in order to address the single-site anisotropy, we compared ferromagnetic calculations). This energy should be compared to the total magnetic stabilization energy (i.e., the energy difference between magnetic and nonmagnetic solutions) of maximally 5 meV. When the DFT calculations are performed including a $U = 2$ eV, the magnetic anisotropy is as large as 8 meV out of a total energy of 28 meV. This substantial anisotropy suggests that a single-site term should be added to the Kitaev-Heisenberg Hamiltonian, probably resulting in a rather different phase diagram.

With all these caveats, it is still instructive to analyze where Na_2IrO_3 is to be found in the parametric space of the nnKH model. We make the following assumptions: (i) that the atomic orbitals are fully localized and the appropriate basis is given by pure $j_{\rm eff} = 1/2$ orbitals; (ii) that the only hoppings relevant for magnetic interactions are pd hoppings, so that the only oxygen-assisted Ir-Ir hoppings are specific t_{2g}-t_{2g} hoppings between unlike orbitals, as outlined in Refs. 2,5, and the t_{2g}-e_g hoppings given in Ref. 4; and (iii) that the only processes contributing to magnetic interactions are those listed in Ref. 4.

Indeed, the fact that the experimentally observed magnetic order is zigzag suggests that either the Heisenberg terms are exceptionally long ranged (the 3rd neighbor exchange is comparable to the 1st one)[7,8] or that the Kitaev term is strong and antiferromagnetic.[4,34] The former suggestion is seemingly in contradiction with the fact that the calculated 3rd neighbor hoppings are substantially smaller than the 1st neighbor ones. This makes it impossible to explain the large 3rd neighbor exchange integral in terms of superexchange. However, there is a possibility, suggested in Ref. 5, that the Ir electrons are itinerant over individual hexagons, which makes magnetic interactions naturally long ranged, and not directly related to the hopping integrals.

The second suggestion, which is the one we will focus on in what follows, was proposed in Ref. 4, namely that of an antiferromagnetic Kitaev term. If strong enough, this could explain the observed magnetic order. Below we consider the expressions presented in Ref. 4 and substitute the unknown variables with *ab initio*–derived parameters.

Chaloupka *et al.*[4] discuss four relevant processes contributing to the exchange interactions in Na_2IrO_3: (1) Direct hopping $t_{1\sigma}$ between nearest neighbor Ir t_{2g} orbitals contributing with a term $I_1 = (\frac{2}{3}t_{1\sigma})^2/U$ to the Heisenberg term, where U is the Coulomb repulsion between t_{2g} electrons.

(2) Interorbital nearest neighbor Ir t_{2g}-e_g hopping via intermediate oxygens $\tilde{t}_1$, with $\tilde{t}_1 = t_{pd\sigma}t_{pd\pi}/\Delta$, where Δ is the charge transfer energy (the difference between the O p and Ir d levels) contributing with a term $I_2 = \frac{4}{9}\frac{\tilde{t}_1^2}{\tilde{U}}\frac{\tilde{J}_{\rm H}}{\tilde{U}}$ both to the Kitaev and Heisenberg terms, but with the opposite signs. Here $\tilde{U}$ is the excitation energy associated with the t_{2g}-e_g hopping; i.e., it also includes crystal field splitting, $\tilde{U} = U + 10Dq$. $\tilde{J}_{\rm H}$ is the Hund's rule coupling between t_{2g} and e_g electrons.

(3) Oxygen-assisted hopping between two nearest neighbor Ir t_{2g} orbitals $t_{1\rm O}$ contributing with a term $I_3 = \frac{8}{3}\frac{t_{1\rm O}^2}{U}\frac{J_{\rm H}}{U}$ to the Kitaev term, where $J_{\rm H}$ is the Hund's rule coupling between t_{2g} electrons, and, we recall, $t_{1\rm O} = t_{pd\pi}^2/\Delta$.

(4) Oxygen-$2p$ – iridium-$5d$ charge transfer contributing with a term $I_4 = \frac{8t_{1\rm O}^2}{9}[\frac{1}{2\Delta+U_p-3J_p} + \frac{1}{3(2\Delta+U_p-J_p)} + \frac{2}{3(2\Delta+U_p+2J_p)} - \frac{1}{\Delta}]$, where U_p and J_p are, respectively, the

Hubbard repulsion and the Hund's rule parameter for oxygen. This expression was derived by G. Khaliullin[35] and is worth some additional discussion. The first three terms correspond to processes where two holes of the same or of opposite spins meet at an oxygen atom. Neglecting J_p, one gets simply $\frac{8t_{1\mathrm{O}}^2}{9}\frac{1}{\Delta+U_p/2}$, which reflects the fact that if the Ir atoms have opposite spins one can create an intermediate state with two holes on the same oxygen orbital, which lowers the total energy. The last term appears due to ring exchange, with an intermediate state where two holes are located on different oxygens. This process is only allowed when the ground state is FM, and only if the ground state hole is in an a_{1g} or $j_{\mathrm{eff}} = 1/2$ state, but not for pure t_{2g} orbitals. However, contrary to a common misconception, J_p is large, between 1.2 and 1.6 eV. We have estimated U_p and J_p, using the technique described in Ref. 37, and obtained $U_p = 2.7$ and $J_p = 1.6$ eV, consistent with earlier DFT estimates.[36] For nonrelativistic orbitals it is comparatively straightforward to account for the Hund's rule coupling on O, but for relativistic orbitals it becomes more tedious.

If we expand I_4 in both U_p and J_p, then $I_4 \approx \frac{8t_{1\mathrm{O}}^2}{9}\frac{U_p-J_p}{2\Delta^2}$. This expression shows that U_p alone contributes ferromagnetically to the Heisenberg term and antiferromagnetically to the Kitaev term and may shift the various phases in the nnKH model. Together with J_p though, for the values suggested above the effect of U_p and J_p largely cancels and I_4 appears to be unimportant (note though that if J_p is entirely neglected, as in Ref. 4, this proposition becomes more questionable).

Summarizing the above terms into a single expression, Eq. (1) can be written as

$$H_{ij}^{(\gamma)} = \underbrace{(2I_2 - I_3 + 2I_4)}_{2K} S_i^\gamma S_j^\gamma + \underbrace{(I_1 - I_2 - I_4)}_{J} \mathbf{S}_i \cdot \mathbf{S}_j. \quad (17)$$

This model has a zigzag magnetic ground state[4] if the Kitaev term is antiferromagnetic (AFM) and the Heisenberg term is ferromagnetic (FM), with $K > 0$, $J < 0$, and $-26 \lesssim K/J \lesssim -0.3$.

In Table IV we provide the parameter values relevant for Na_2IrO_3, as obtained from our DFT results. Note that the $\tilde{t}_1$ parameter was assumed to be $2t_{1\mathrm{O}}$ in Ref. 4, while in the calculations (DFT calculations are usually very reliable in this respect) $\tilde{t}_1/t_{1\mathrm{O}}$ is 1.4. However, using the ratio of 2 hardly changes any conclusions.

TABLE IV. DFT-calculated values of transfer integrals and charge transfer energy between the O p and Ir d levels for Na_2IrO_3 and estimates of Hund's rule coupling strength as described in the text. The values marked with * were obtained from $\tilde{t}_1$, $t_{1\mathrm{O}}$ and Δ.

Parameter	Value (eV)	Meaning
$t_{1\sigma}$	0.03	direct Ir-Ir hopping
$t_{1\mathrm{O}}$	0.27	O-assisted Ir-Ir hopping
$\tilde{t}_1$	0.38	Ir t_{2g}-e_g hopping
$t_{pd\pi}$	0.57*	Ir-O π hopping
$t_{pd\sigma}$	1.6*	Ir-O σ hopping
Δ	2.4	charge transfer energy between the O p and Ir d levels
J_{H}	0.5	Ir t_{2g} Hund's rule coupling
$\tilde{J}_{\mathrm{H}}$	0.5	Ir t_{2g}-e_g Hund's rule coupling

We present our results in Figs. 9 and 10. In Fig. 9 we show the calculated values of K and J as a function of two variables: the x axis is the Hubbard U associated with the upper Kramers doublet, and the y axis is the energy $\tilde{U}$, associated with exciting an individual electron from the upper t_{2g} to an average e_g state. The Hubbard U for $5d$ electrons is, generally speaking, 1.5 to 2 eV. However, in this case it is additionally screened by the e_g electrons, and also reduced by hybridization (cf. Na_xCoO_2[38] and Fe pnictides[39]). Experimental estimates of the Hubbard U defined as the energy cost for exciting electrons across the insulating gap (which is the definition relevant to superexchange) yield 0.3–0.5 eV.[11,33] Additionally, LDA + U calculations with $U \sim 2$ eV yield an excitation gap of the same order. We conclude that the realistic range of this parameter is 0.5–2 eV, with the smaller values more likely.

For the second parameter, $\tilde{U}$, DFT calculations give $\sim$2.5 eV. This should be considered as a lower bound since DFT tends to slightly overestimate the orbital overlap and crystal fields, and misses the effects of the t_{2g}-e_g Hubbard interaction. One can thus limit the physically admissible range in the region 2.5 eV $\lesssim \tilde{U} \lesssim$ 3 eV.

In Fig. 10 we show the phase diagram in the space of the two parameters above. Several observations are in place: (1) While there is a zigzag phase in this diagram, it is very far removed from the range of the parameters that can be called physical, 0.5 eV $\lesssim U \lesssim$ 2 eV, 2 eV $\lesssim \tilde{U} \lesssim$ 3 eV (even though in the above estimate we have liberally stretched the admissible range in favor of a zigzag phase). In fact, the zigzag regime appears only when $\tilde{U} < 0.6U$, i.e., when the Hubbard gap is larger than the e_g-t_{2g} splitting, a rather unlikely proposition. (2) In the physical range of parameters, the ground state is either ferromagnetic or the spin liquid phase. It is rather curious that the very narrow slivers of the phase space in the J,K coordinates[4] are transformed into a very large range in the $U,\tilde{U}$ space.

It is also worth mentioning that in order to explain the experimental data of Refs. 7,8 one needs not only the ground state to be zigzag, but also that K be several times larger than $|J|$; Chaloupka *et al.*[4] used $K = 10.44$ and $J = -4.01$ meV. This solution cannot be obtained for a given set of U and $\tilde{U}$ (see Fig. 9). Moreover, a closer look at the expressions in their work reveals that $K + J = I_1 - I_3/2$, which does not depend on $\tilde{U}$ and is always negative. Thus the two equalities above cannot be satisfied simultaneously for any choice of parameters, be they physical or not. Moreover, the values of J and K used in Ref. 4 can only be obtained if $\tilde{U} < 0.2$ eV, which is clearly an impossible regime.

B. Long-range exchange

As mentioned above, an alternative interpretation of the experimental results, given in Refs. 7,8, is in terms of sizable 2nd and 3rd neighbor exchange constants, comparable to the nearest neighbor exchange. In this picture the Kitaev term may or may not play a role, but this role is not decisive in establishing the observed magnetic order. Given that the calculated hopping amplitudes (Table I) are clearly dominated by the nearest neighbor terms, standard superexchange cannot explain such long-range interactions.

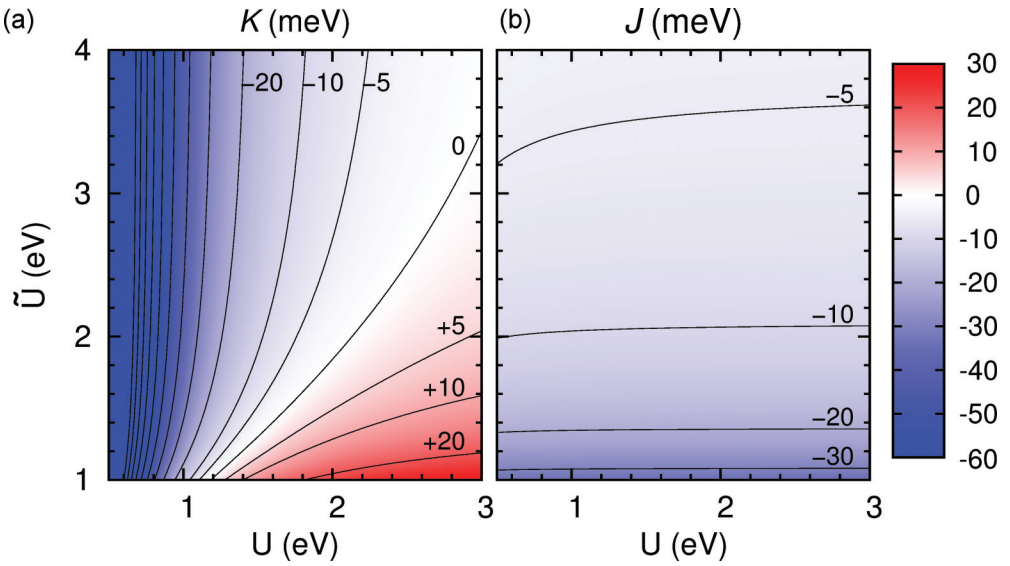

FIG. 9. (Color online) Variation of (a) Kitaev parameter K and (b) Heisenberg exchange coupling J with on-site Coulomb coupling strength U and Ir t_{2g}-e_g excitation energy $\tilde{U}$. Positive values refer to antiferromagnetic, negative to ferromagnetic values of K and J. The other parameters entering the K and J are given in Table IV A.

However, it is important to remember that in the opposite, itinerant limit every electron is fully delocalized over a hexagon and, as such, is equally sensitive to the mean-field magnetization pattern on the 1st, 2nd, or 3rd nearest neighbors. As discussed in our earlier work,[5] the zigzag order, as compared to the stripy one, results in a sizable pseudogap at the Fermi level even without a Hubbard U. This creates an energy gain that cannot be cast in a form of nearest neighbor interaction, as it depends on the magnetization pattern over an entire hexagon.

We are far from stating that the superexchange Hamiltonian outlined in Ref. 4 is irrelevant and an itinerant description will give the final answer to all questions regarding the magnetism in Na_2IrO_3. However, relying solely on the localized picture and, correspondingly, on the nnKH model, is, apparently, inadequate.

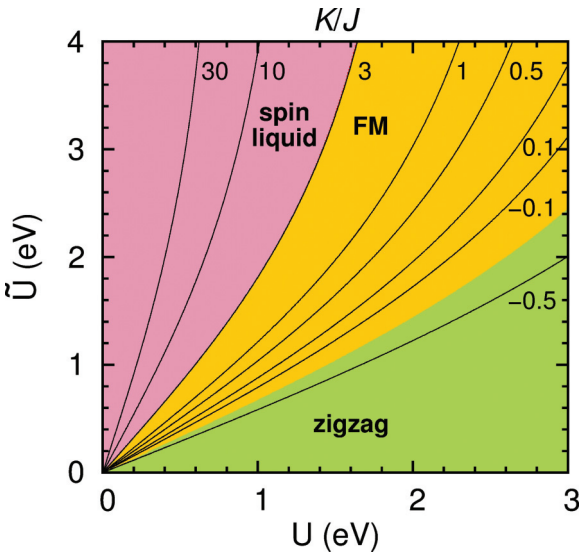

FIG. 10. (Color online) Phase diagram of the Kitaev-Heisenberg model for Na_2IrO_3 with parameters determined following Ref. 4. The calculated exchange integrals are functions of the Mott-Hubbard gap U and the cubic crystal field splitting $\tilde{U}$. The contours mark isolines of the ratio K/J.

VII. CONCLUSIONS

In summary, we have performed an extensive investigation of the electronic properties of Na_2IrO_3 in the framework of nonrelativistic and relativistic density functional theory calculations and derived by means of the Wannier function projector method, the corresponding microscopic parameters. We resolved the following open questions: (1) By considering various idealized crystal structures for Na_2IrO_3 we could disentangle the effect of each of the structural distortions present in this system and concluded that it is the joint effect of these distortions that constructively enhances the intrahexagon effective hopping parameters and suppresses the interhexagon ones favoring the formation of quasimolecular orbitals. (2) We modeled the relativistic DFT results in terms of a tight-binding model including the spin-orbit coupling term and analyzed the electronic properties of Na_2IrO_3 in terms of two complementary descriptions, the (itinerant) quasimolecular basis and the (localized) relativistic j_{eff} basis. We observed that the behavior of Na_2IrO_3 lies in between the fully itinerant and the fully localized description and that a quasimolecular orbital description keeps its character even at large values of the spin-orbit coupling strength. (3) We showed that XAS and RIXS observations can be well understood within an itinerant description of Na_2IrO_3 in contrast to other iridates such as Sr_3CuIrO_6 where localization is imposed by the crystallographic arrangement of the IrO_6 octahedra.[40] (4) Finally, we provided *ab initio*–derived estimates for the parameters appearing in the Kitaev and Heisenberg terms in Na_2IrO_3 and found that the recently proposed nnKH model (see Sec. VI), even though it is a very interesting model *per se*, is unfortunately not realistic for Na_2IrO_3. In conclusion,

in order to obtain a full understanding of the behavior of Na_2IrO_3 all three features—spin-orbit, Coulomb correlations, and delocalization of valence electrons over Ir_6 hexagons—are essential.

ACKNOWLEDGMENTS

H.O.J., D.Kh., and R.V. acknowledge support by the Deutsche Forschungsgemeinschaft through Grants No. SFB/TR 49 and No. FOR 1346 (H.O.J. and R.V.), and No. SFB 608 and No. FOR 1346 (D.Kh.).

APPENDIX: IDEALIZED Na_2IrO_3 CRYSTAL STRUCTURES AS USED IN WIEN2k

1. Experimental structure from Ref. 8

Space group $C2/m$ (No. 12)			
$a = 5.4269$ Å,	$b = 6.4104$ Å,	$c = 9.3949$ Å,	$\gamma = 124.12°$
Atom	x	y	z
Na1	0.0	0.0	0.5
Na2	0.5	0.5	0.0
Na3	0.5	0.5	0.3400
Ir	0.0	0.0	0.1670
O1	0.4590	0.2110	0.1780
O2	0.0070	0.7960	0.0

2. Idealized structure S_1

Space group $C2/m$ (No. 12)			
$a = 5.4501$ Å,	$b = 6.4411$ Å,	$c = 9.4399$ Å,	$\gamma = 125.26°$
Atom	x	y	z
Na1	0.0	0.0	0.5
Na2	0.5	0.5	0.0
Na3	0.5	0.5	0.3333
Ir	0.0	0.0	0.1667
O1	0.4646	0.2097	0.1785
O2	0.0000	0.7903	0.0

3. Idealized structure S_2

Space group $C2/m$ (No. 12)			
$a = 5.4501$ Å,	$b = 6.4190$ Å,	$c = 9.4399$ Å,	$\gamma = 124.47°$
Atom	x	y	z
Na1	0.0	0.0	0.5
Na2	0.5	0.5	0.0
Na3	0.5	0.5	0.3333
Ir	0.0	0.0	0.1667
O1	0.4606	0.1909	0.1667
O2	0.0000	0.8091	0.0

4. Idealized structure S_3

Space group $C2/m$ (No. 12)			
$a = 5.0658$ Å,	$b = 5.9869$ Å,	$c = 8.7743$ Å,	$\gamma = 125.26°$
Atom	x	y	z
Na1	0.0	0.0	0.5
Na2	0.5	0.5	0.0
Na3	0.5	0.5	0.3333
Ir	0.0	0.0	0.1667
O1	0.5000	0.2443	0.1667
O2	0.0000	0.7557	0.0

Note that due to the necessity of using a monoclinic angle γ in WIEN2k, the Ir honeycomb layers in the Na_2IrO_3 unit cells presented above are parallel to the ac plane. Accordingly, within this convention the vector of the Bloch factors in Eqs. (4) and (7) is given by

$$T_{M=1\ldots6}(\mathbf{k}) = (1, e^{-ik_x\tilde{a}}, e^{ik_z\tilde{c}}, e^{i(k_z\tilde{c}-k_x\tilde{a})}, e^{ik_z\tilde{c}}, e^{-ik_x\tilde{a}}), \qquad \text{(A1)}$$

where $\tilde{a}$ and $\tilde{c}$ are the lengths of the two primitive lattice vectors lying in the ac plane. Here, one explicitly accounts for the choice of WIEN2k of the actual positions of the two Ir atoms in the primitive unit cell, which are, e.g., $(-0.167,0,0.167)$ and $(-0.833,0,0.833)$ in the experimental Na_2IrO_3 structure.

[1] B. J. Kim, H. Ohsum, T. Komesu, S. Sakai, T. Morita, H. Takagi, and T. Arima, Science **323**, 1329 (2009).

[2] J. Chaloupka, G. Jackeli, and G. Khaliullin, Phys. Rev. Lett. **105**, 027204 (2010).

[3] J. Reuther, R. Thomale, and S. Trebst, Phys. Rev. B **84**, 100406(R) (2011).

[4] J. Chaloupka, G. Jackeli, and G. Khaliullin, Phys. Rev. Lett. **110**, 097204 (2013).

[5] I. I. Mazin, H. O. Jeschke, K. Foyevtsova, R. Valentí, and D. I. Khomskii, Phys. Rev. Lett. **109**, 197201 (2012). Please note that the corresponding B_{1u} eigenenergy in Table I of this publication should read $-2(t_1' - t_2')$ and the upper two levels merge at $|t_1'/t_2'| = 3$. Note that t_1' and t_2' are labeled $t_{1\,O}$ and $t_{2\,O}$ respectively in the present work.

[6] The spin-orbit splitting is given by the difference of the eigenvalues $\lambda/2$ and $-\lambda$ in the j_{eff} space.

[7] Y. Singh, S. Manni, J. Reuther, T. Berlijn, R. Thomale, W. Ku, S. Trebst, and P. Gegenwart, Phys. Rev. Lett. **108**, 127203 (2012).

[8] S. K. Choi, R. Coldea, A. N. Kolmogorov, T. Lancaster, I. I. Mazin, S. J. Blundell, P. G. Radaelli, Y. Singh, P. Gegenwart, K. R. Choi, S.-W. Cheong, P. J. Baker, C. Stock, and J. Taylor, Phys. Rev. Lett. **108**, 127204 (2012).

[9] From these considerations, one can think of other materials with basically the same structure, in which 1/3 of the in-plane *foreign* atoms M in $Na(M_{1/3}Ir_{2/3})O_2$ can be any metal M. Such a program was recently realized by the group of R. J. Cava (private communication).

[10]Y. Singh and P. Gegenwart, Phys. Rev. B **82**, 064412 (2010).
[11]R. Comin, G. Levy, B. Ludbrook, Z.-H. Zhu, C. N. Veenstra, J. A. Rosen, Y. Singh, P. Gegenwart, D. Stricker, J. N. Hancock, D. van der Marel, I. S. Elfimov, and A. Damascelli, Phys. Rev. Lett. **109**, 266406 (2012).
[12]P. Blaha, K. Schwarz, G. K. H. Madsen, D. Kvasnicka, and J. Luitz, WIEN2k, *An Augmented Plane Wave + Local Orbitals Program for Calculating Crystal Properties* (Karlheinz Schwarz, Techn. Universität Wien, Austria, 2001).
[13]J. P. Perdew, K. Burke, and M. Ernzerhof, Phys. Rev. Lett. **77**, 3865 (1996).
[14]S. Cottenier, *Density Functional Theory and the Family of (L)APW Methods: A Step-by-Step Introduction* (Instituut voor Kern- en Stralingsfysica, K. U. Leuven, Belgium, 2002), to be found at http://www.wien2k.at/reg_user/textbooks.
[15]M. Aichhorn, L. Pourovskii, V. Vildosola, M. Ferrero, O. Parcollet, T. Miyake, A. Georges, and S. Biermann, Phys. Rev. B **80**, 085101 (2009).
[16]J. Ferber, K. Foyevtsova, H. O. Jeschke, and R. Valentí, arXiv:1209.4466.
[17]The description of the orbital character in the present work is done according to the local cubic coordinate system if not explicitly specified otherwise.
[18]K. Koepernik and H. Eschrig, Phys. Rev. B **59**, 1743 (1999); http://www.FPLO.de.
[19]In Fig. 6 we visualize real-valued combinations of degenerate E_{2u} or E_{1g} QMOs.
[20]We compared our prepared idealized structures to those provided by Radu Coldea (private communication) and the agreement between both sets of structures is very good.
[21]C. Martins, M. Aichhorn, L. Vaugier, and S. Biermann, Phys. Rev. Lett. **107**, 266404 (2011).
[22]A. Shitade, H. Katsura, J. Kuneš, X.-L. Qi, S.-C. Zhang, and N. Nagaosa, Phys. Rev. Lett. **102**, 256403 (2009).
[23]Note that these states are eigenstates of Eq. (6) after diagonalizing the matrix Eq. (6) and performing an appropriate rotation.
[24]Orthorhombic distortion lifts the degeneracy of the E_{1g} and E_{2u} states combining them into real functions.
[25]In the ideal case, one would have, e.g., $B_{1u}\uparrow = (-0.408, -0.408, -0.408, 0.408, 0.408, 0.408, 0.408, 0, 0, 0, 0, 0, 0, 0)$.
[26]D. Haskel, G. Fabbris, M. Zhernenkov, P. P. Kong, C. Q. Jin, G. Cao, and M. van Veenendaal, Phys. Rev. Lett. **109**, 027204 (2012).
[27]L. C. Chapon and S. W. Lovesey, J. Phys.: Condens. Matter **23**, 252201 (2011).
[28]S. W. Lovesey and A. N. Dobrynin, J. Phys.: Condens. Matter **24**, 382201 (2012).
[29]S. W. Lovesey, D. D. Khalyavin, P. Manuel, L. C. Chapon, G. Cao, and T. F. Qi, J. Phys.: Condens. Matter **24**, 496003 (2012).
[30]G. van der Laan and B. T. Thole, Phys. Rev. Lett. **60**, 1977 (1988).
[31]B. T. Thole and G. van der Laan, Phys. Rev. B **38**, 3158 (1988).
[32]J. P. Clancy, N. Chen, C. Y. Kim, W. F. Chen, K. W. Plumb, B. C. Jeon, T. W. Noh, and Y.-J. Kim, Phys. Rev. B **86**, 195131 (2012).
[33]H. Gretarsson, J. P. Clancy, X. Liu, J. P. Hill, E. Bozin, Y. Singh, S. Manni, P. Gegenwart, J. Kim, A. H. Said, D. Casa, T. Gog, M. H. Upton, H.-S. Kim, J. Yu, V. M. Katukuri, L. Hozoi, J. van den Brink, and Y.-J. Kim, Phys. Rev. Lett. **110**, 076402 (2013).
[34]Y. Yu, L. Liang, Q. Niu, and S. Qin, Phys. Rev. B **87**, 041107(R) (2013).
[35]G. Khaliullin (private communication).
[36]I. I. Mazin and D. J. Singh, Phys. Rev. B **56**, 2556 (1997).
[37]A. G. Petukhov, I. I. Mazin, L. Chioncel, and A. I. Lichtenstein, Phys. Rev. B **67**, 153106 (2003).
[38]H. Ishida, M. D. Johannes, and A. Liebsch, Phys. Rev. Lett. **94**, 196401 (2005).
[39]See, for instance, M. Aichhorn, L. Pourovskii, and A. Georges, Phys. Rev. B **84**, 054529 (2011).
[40]X. Liu, Vamshi M. Katukuri, L. Hozoi, W.-G. Yin, M. P. M. Dean, M. H. Upton, J. Kim, D. Casa, A. Said, T. Gog, T. F. Qi, G. Cao, A. M. Tsvelik, J. van den Brink, and J. P. Hill, Phys. Rev. Lett. **109**, 157401 (2012).